Published in final edited form as:

Cell Rep. 2020 August 18; 32(7): 108039. doi:10.1016/j.celrep.2020.108039.

Proteolytic Restriction of Chordin Range Underlies BMP Gradient Formation

Francesca B. Tuazon[1], **Xu Wang**[2,3], **Jonathan Lee Andrade**[1], **David Umulis**[2,3,*], **Mary C. Mullins**[1,4,*]

[1]Department of Cell and Developmental Biology, University of Pennsylvania Perelman School of Medicine, Philadelphia, PA 19104, USA

[2]Department of Agriculture and Biological Engineering, Purdue University, West Lafayette, IN 47907, USA

[3]Weldon School of Biomedical Engineering, Purdue University, West Lafayette, IN 47907, USA

[4]Lead Contact

SUMMARY

A fundamental question in developmental biology is how morphogens, such as bone morphogenetic protein (BMP), form precise signaling gradients to impart positional and functional identity to the cells of the early embryo. We combine rigorous mutant analyses with quantitative immunofluorescence to determine that the proteases Bmp1a and Tolloid spatially restrict the BMP antagonist Chordin in dorsoventral (DV) axial patterning of the early zebrafish gastrula. We show that maternally deposited Bmp1a plays an unexpected and non-redundant role in establishing the BMP signaling gradient, while the Bmp1a/Tolloid antagonist Sizzled is surprisingly dispensable. Combining computational modeling and *in vivo* analyses with an immobile Chordin construct, we demonstrate that long-range Chordin diffusion is not necessary for BMP gradient formation and DV patterning. Our data do not support a counter-gradient of Chordin and instead favor a Chordin sink, established by Bmp1a and Tolloid, as the primary mechanism that drives BMP gradient formation.

Graphical Abstract

*Correspondence: dumulis@purdue.edu (D.U.), mullins@pennmedicine.upenn.edu (M.C.M.).

AUTHOR CONTRIBUTIONS

Conceptualization, F.B.T., D.U., and M.C.M.; Methodology, F.B.T., X.W., D.U., and M.C.M.; Software, F.B.T., X.W., and D.U.; Validation, F.B.T., X.W., J.L.A., D.U., and M.C.M.; Formal Analysis, F.B.T., X.W., J.L.A., D.U., and M.C.M.; Investigation, F.B.T., X.W., J.L.A., D.U., and M.C.M.; Data Curation, F.B.T., X.W., and D.U.; Writing – Original Draft, F.B.T., X.W., D.U., and M.C.M.; Writing – Review & Editing, F.B.T., X.W., J.L.A., D.U., and M.C.M.; Visualization, F.B.T., X.W., D.U., and M.C.M.; Supervision, D.U. and M.C.M.; Project Administration, D.U. and M.C.M.; Funding Acquisition, F.B.T., D.U., and M.C.M.

SUPPLEMENTAL INFORMATION

Supplemental Information can be found online at https://doi.org/10.1016/j.celrep.2020.108039.

DECLARATION OF INTERESTS

The authors declare no competing interests.

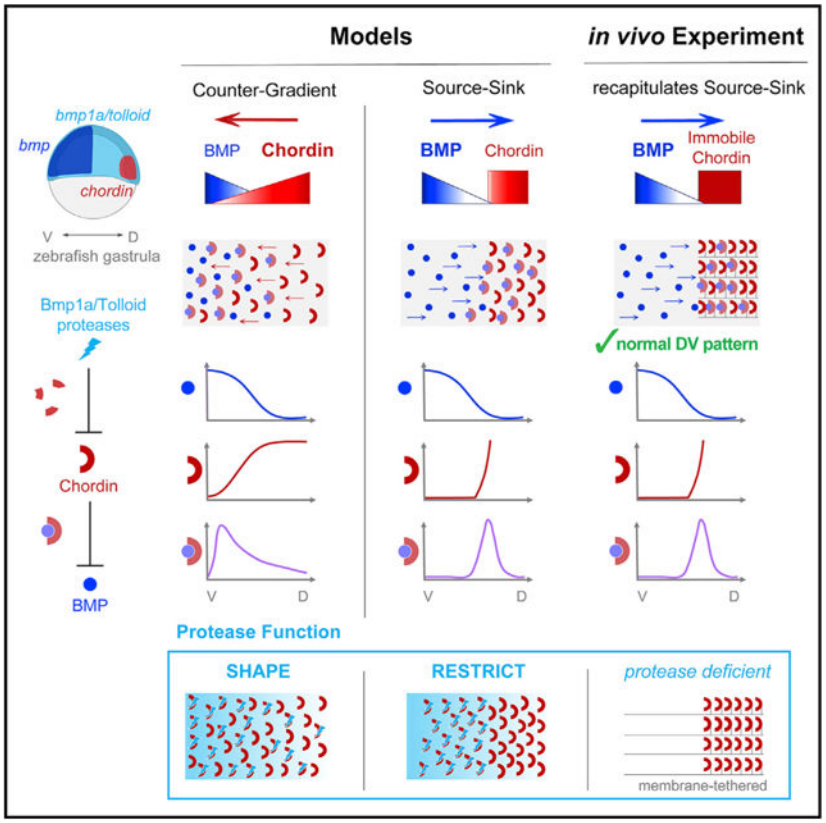

In Brief

The BMP morphogen generates a precise signaling gradient during axial patterning. In the zebrafish embryo, Tuazon et al. find that proteases Bmp1a/Tolloid are key to this process, preventing the long-range diffusion of the BMP antagonist, Chordin. By regionally restricting Chordin, Bmp1a/Tolloid establish the signaling sink that drives BMP gradient formation.

INTRODUCTION

A fundamental question of developmental biology is how the un-patterned cells of the early embryo gain the positional and functional identity necessary to generate a mature organism (Wolpert, 1969). In this process, distinct cell fates are specified by morphogens, signaling factors that form spatial gradients to direct cell fate in a concentration-dependent manner (Ashe and Briscoe, 2006; Briscoe and Small, 2015; Rogers and Schier, 2011). Morphogens direct initial patterning of the pluripotent cells of the early embryo, as well as tissue and organ patterning later in development (Sansom and Livesey, 2009; Tuazon and Mullins, 2015). Furthermore, these developmental signaling molecules are often re-used during injury repair and exploited in disease progression. Thus, uncovering the mechanisms that generate and regulate morphogen gradients has broad implications to our understanding of both development and disease. Bone morphogenetic proteins (BMPs) act as a morphogen to pattern the embryonic dorsoventral (DV) axis of all vertebrates (Bier and De Robertis, 2015; Tuazon and Mullins, 2015; Zinski et al., 2018) and are later repurposed to direct neural tube

and digit patterning (Dutko and Mullins, 2011; Suzuki et al., 2008; Zagorski et al., 2017). Here, we investigate mechanisms underlying BMP patterning of the zebrafish DV axis.

BMP is a secreted transforming growth factor β (TGF-β) family ligand that binds and activates its transmembrane receptor complex to phosphorylate the Smad5 (P-Smad5) transcription factor (Zinski et al., 2018) (Figure 1A). P-Smad5 subsequently accumulates in the nucleus and induces BMP target genes (Hild et al., 1999; Massagué et al., 2005; Schmierer and Hill, 2007). The gradient of BMP ligand is regulated extracellularly by various secreted modulators (Little and Mullins, 2006; Umulis et al., 2009; Zakin and De Robertis, 2010; Zinski et al., 2018). The central BMP antagonist is Chordin, which binds and sequesters BMP ligand to prevent signaling (Piccolo et al., 1996; Schulte-Merker et al., 1997; Troilo et al., 2014). Chordin function is modulated by two additional classes of proteins: (1) the metalloproteases Bmp1a and Tolloid, which cleave and inactivate Chordin (Blader et al., 1997; Jasuja et al., 2007; Muraoka et al., 2006; Piccolo et al., 1997; Wardle et al., 1999); and (2) the metalloprotease inhibitor Sizzled, which binds the active site of Bmp1a and Tolloid to prevent them from cleaving Chordin (Lee et al., 2006; Muraoka et al., 2006) (Figure 1A). These genes are expressed in distinct domains: *bmp* and *sizzled* ventrally (Schmid et al., 2000; Yabe et al., 2003), *chordin* dorsally (Schulte-Merker et al., 1997), and *bmp1a* and *tolloid* ubiquitously (Connors et al., 1999; Jasuja et al., 2007; Muraoka et al., 2006) (Figure 1A′). In vertebrates, a BMP signaling gradient specifies ventral cell fates (e.g., epidermis, blood) at high levels and lateral fates (e.g., neural crest) at intermediate levels, while dorsal fates (e.g., neural tissue) result from no BMP signaling (Bier and De Robertis, 2015; Heasman, 2006; Schier and Talbot, 2005; Tuazon and Mullins, 2015) (Figure 1A″).

The roles of Bmp1a, Tolloid, and Sizzled in generating the zebrafish BMP gradient warrant further investigation. Bmp1a and Tolloid likely have partially redundant functions since their amino acid sequences are highly similar (93.4%) (Figure S1A) and their expression domains overlap, though *bmp1a* alone is maternally deposited (Figures 1A′ and 1B) (Connors et al., 1999; Jasuja et al., 2006; Muraoka et al., 2006; Xie and Fisher, 2005). However, the extent of Bmp1a/Tolloid redundancy during BMP gradient formation, and any impact Sizzled may have on it, was unclear. To this end, we utilized a quantitative immunofluorescence approach that we recently developed to quantify nuclear P-Smad5, the direct intracellular readout of BMP signaling (Figure 1A). We can visualize the P-Smad5 gradient at single-cell resolution embryo-wide and compare differences across mutant populations (Zinski et al., 2017, 2019), providing the comprehensive, high-resolution analysis required to determine the spatial and temporal contributions of Bmp1a, Tolloid, and Sizzled.

Furthermore, we combined our quantitative P-Smad5 analysis with mathematical modeling and large-scale computational screens to distinguish among proposed mechanisms of BMP gradient formation. The predominant model in the field has been a counter-gradient mechanism, where dorsally secreted Chordin diffuses ventrally in an embryo-wide gradient generating an inverse gradient of BMP signaling (Figure 1C) (De Robertis and Moriyama, 2016; Plouhinec et al., 2013). We recently excluded two alternative models of BMP gradient formation by computational modeling in zebrafish: a mechanism that relies on a gradient of *bmp* transcript and a mechanism acting in *Drosophila* DV patterning relying on facilitated

BMP diffusion with Chordin (Zinski et al., 2017). The final remaining model is a source-sink mechanism, where BMP diffuses from its source ventrally to be captured by a regionally limited sink of Chordin dorsally (Figure 1C) (Zinski et al., 2017). The key distinction between the counter-gradient and source-sink mechanisms is what drives BMP gradient formation: in the counter-gradient, it is long-range Chordin diffusion across the embryo, while in the source sink, it is the diffusion of BMP itself, and Chordin range must remain limited (Figure 1C, arrows). However, since both BMP and Chordin rapidly diffuse (Inomata et al., 2013; Pomreinke et al., 2017; Zinski et al., 2017), both a Chordin counter-gradient and a Chordin sink remained viable mechanisms for BMP gradient formation, and how a dorsal sink of Chordin could be established was unknown.

Here, we combined rigorous maternal-zygotic (MZ) double-mutant analyses with P-Smad5 quantitation to determine that Bmp1a and Tolloid are required to spatially restrict Chordin in the early zebrafish gastrula. We discovered that maternally deposited Bmp1a plays an unexpected and non-redundant role in establishing the BMP gradient, while Sizzled is surprisingly dispensable. Incorporating Bmp1a, Tolloid, and Sizzled into a computational modeling screen of zebrafish BMP gradient formation revealed that despite its high diffusivity, Chordin has a limited effective range. We found no modeling solutions consistent with the counter-gradient mechanism, and instead the solutions favor a restricted Chordin sink, generated by Bmp1a and Tolloid. We directly tested this by regionally expressing an immobile Chordin construct in embryos deficient in Bmp1a, Tolloid, and endogenous Chordin. Remarkably, immobile Chordin was able to pattern the DV axis of these embryos, consistent with our model that Bmp1a and Tolloid proteases are key to restrict Chordin and establish the sink that drives BMP gradient formation.

RESULTS

Loss of Maternal *bmp1a* Increases tolloid Mutant DV Patterning Defects

Previous studies evaluating Bmp1a relied solely on morpholino (MO)-mediated knockdown of *bmp1a* and had conflicting phenotypes: one found no DV patterning defects (Jasuja et al., 2006), while the other reported severe dorsalization, lysis, and death (Muraoka et al., 2006). To resolve this discrepancy and circumvent any non-specific MO effects, we utilized two nonsense mutations: $bmp1a^{t31169}$, a characterized null (Bowen et al., 2012); and $bmp1a^{sa2416}$, from the Zebrafish Mutation Project (Kettleborough et al., 2013) (Figure S1A). We generated MZ mutant embryos of each allele, and both displayed a wild-type phenotype at 36 h post-fertilization (hpf) (Figures 1D and S1B), concurring that *bmp1a* loss has no apparent effect on DV patterning (Jasuja et al., 2006). $bmp1a^{sa2416}$ mutants phenocopied $bmp1a^{t31169}$, displaying a ruffled tail fin by 5 days post-fertilization (dpf) and adult craniofacial, tail, and body axis defects (Figures S1B–S1D), consistent with its later role in skeletal development and unrelated to DV patterning (Asharani et al., 2012; Bowen et al., 2012; Gistelinck et al., 2018; Hur et al., 2017). The remaining experiments use the $bmp1a^{t31169}$ allele unless otherwise noted.

We evaluated whether Bmp1a and Tolloid function redundantly during DV patterning by generating double-mutant embryos with zygotic (Z), maternal (M), or MZ loss of *bmp1a* (Figure 1E). Double zygotic mutants were generated by intercrossing *bmp1a;tolloid* double

heterozygotes (Figure 1E). Dorsalized progeny were classified on an established scale, with C1 being mild and C5 being most severe (Mullins et al., 1996), and subsequently genotyped for *bmp1a* and *tolloid*. Since not all progeny were dorsalized, a subset of wild-type embryos was genotyped (Figure 1F, columns 1–3). Single Z-*bmp1a* homozygotes were wild type, and additional heterozygosity for *tolloid* had no effect (Figure 1F, columns 2 and 3). In contrast, single *tolloid* homozygotes were C1, and additional heterozygosity for *bmp1a* resulted in mostly C2 phenotypes (Figures 1D and 1F, columns 4 and 5). Homozygous *bmp1a;tolloid* double mutants were C3 dorsalized, a moderately severe phenotype, indicating that zygotic *bmp1a* and *tolloid* function redundantly (Figures 1F, column 6, S1E, and S1F).

We generated embryos lacking maternal *bmp1a* and zygotic *tolloid* (M-*bmp1a;tolloid*) by crossing a female homozygous for *bmp1a* and heterozygous for *tolloid* with a male heterozygous for *tolloid* (Figure 1E). Strikingly, all M-*bmp1a;tolloid* embryos were the most severe C5 dorsalization phenotype, while siblings remained wild type (Figure 1F, columns 7–9). We confirmed that C5 embryos were radially dorsalized by wholemount *in situ* analysis of neurectoderm markers *pax2.1* (mid-hindbrain boundary) and *krox20* (hindbrain rhombomeres 3 and 5). Expression of *pax2.1* and *krox20* is normally restricted dorsally; however, in the majority of M-*bmp1a;tolloid* embryos, these markers were expanded around the entire embryo (Figure 1G). We saw the same phenotype when injecting an antisense MO targeting *tolloid* (*tll1*MO) (Kok et al., 2015; Lele et al., 2001) into M-*bmp1a* embryos (Figures S2A and S2B). The same concentration of *tll1*MO that phenocopied *tolloid* mutants when injected into wild-type embryos (Figure S2A) caused C5 radial dorsalization in M-*bmp1a* embryos (Figures S2A and S2B). These data indicate that maternally deposited *bmp1a* alone is redundant with *tolloid*, and both are absolutely required to pattern the DV axis.

Finally, we generated embryos lacking maternal-zygotic *bmp1a* and zygotic *tolloid* (MZ-*bmp1a;tolloid*) by crossing a female homozygous for *bmp1a* and heterozygous for *tolloid* with a *bmp1a;tolloid* double heterozygous male (Figure 1E). All MZ-*bmp1a;tolloid* embryos were C5 dorsalized, while MZ-*bmp1a* siblings remained wild type (Figure 1F, columns 10 and 12). As with Z-*bmp1a* and M-*bmp1a*, additional heterozygosity for *tolloid* had no effect on MZ-*bmp1a* embryos (Figure 1F, column 11). Furthermore, in MZ-*bmp1a* embryos injected with *tll1*MO, *chordin* expression remained unchanged (Figure S2C), which excludes that an expanded *chordin* expression domain contributes to the observed dorsalization. Together with the Z-*bmp1a;tolloid* and M-*bmp1a;tolloid* phenotypes, these data reveal that maternally deposited *bmp1a* is primarily redundant with *tolloid*, and Bmp1a/Tolloid are essential for BMP signaling and DV patterning.

Bmp1a/Tolloid Shield BMP Signaling from Chordin Embryo-wide

To understand how Bmp1a/Tolloid shape the BMP signaling gradient, we quantified P-Smad5 in all nuclei of the early gastrula at 5.7 hpf, when the wild-type gradient is firmly established (Zinski et al., 2017, 2019) (Figure 2A). We found that loss of M- or MZ-Bmp1a and Tolloid caused a dramatic loss of P-Smad5 across the embryo (Figures 2B and S2D–S2G), consistent with their radial dorsalization (Figures 1F and 1G). We quantified P-Smad5 levels around the embryo margin (Figure 2C) and compared the distribution in the loss-of-

function conditions to the wild type. We found that the P-Smad5 gradient in embryos deficient for both maternal Bmp1a and zygotic Tolloid activity is effectively ablated, even in the ventral-most regions where BMP is produced (Figures 2D and S2H). These results indicate that without Bmp1a/Tolloid, Chordin can reach the ventral-most regions of the embryo and inhibit all BMP signaling there. This suggests that a key function of Bmp1a/Tolloid is to restrict Chordin to protect BMP signaling ventrolaterally (Figure 2E).

Bmp1a Alone Modulates the Early BMP Signaling Gradient and DV Patterning

We also quantified the P-Smad5 gradient in both *tolloid* and *bmp1a* single-mutant embryos. *tolloid* mutants are mildly dorsalized, with the phenotype restricted to the tail (Figure 1D) (Connors et al., 1999). While previous work indicates that BMP signaling patterns the tail at the end of gastrulation (9–10 hpf) (Connors et al., 2006; Pyati et al., 2005; Tucker et al., 2008), an earlier change in the P-Smad5 gradient could affect tail patterning (Agathon et al., 2003). However, *tolloid* mutants displayed a wild-type P-Smad5 gradient at 5.7 hpf (early gastrula) (Figures 2F and 2G). This indicates that Tolloid alone does not contribute to BMP gradient formation and that Bmp1a is sufficient at this stage.

In contrast, the P-Smad5 gradients of M- and MZ-*bmp1a* mutant embryos were wholly unexpected. Given that MZ-*bmp1a* mutants exhibit a wild-type phenotype (Figure 1D) and are viable and fertile through multiple generations as adults, we expected to see a wild-type P-Smad5 gradient. However, M- and MZ-*bmp1a* embryos displayed a significantly reduced P-Smad5 gradient at 5.7 hpf (Figures 2H and 2H′). They were compared to stage-matched wild-type controls, which were stained and processed in the same tube as mutants and identified by genotyping after P-Smad5 imaging (indicated by asterisk in all figures). At the margin, where peak P-Smad5 levels were observed (Figure 2C) (Tucker et al., 2008; Zinski et al., 2017), M- and MZ-*bmp1a* embryos exhibited similar P-Smad5 gradients that were both shallower and lower in amplitude than the wild type (Figures 2I, S3A, and S3B). More animally, M-*bmp1a* embryos exhibited higher ventral P-Smad5 intensities than MZ-*bmp1a*, though both gradients were still greatly reduced compared to the wild type (Figure 2I′). Consistent with their reduced P-Smad5 gradients, M-*bmp1a* embryos displayed DV patterning defects, with a loss of ventral marker *gata2* and concomitant expansion of dorsal marker *foxb1a* (Figures 2J and 2J′). Together, these results show that M-Bmp1a alone plays a key role in establishing the BMP gradient and in DV patterning (Figure 2E).

Surprisingly, we found that embryos derived from M-*bmp1a*/+ heterozygous females (crossed to wild-type males) also displayed a significantly reduced P-Smad5 gradient (Figures S3F and S3H). Further, this gradient closely resembled that of M-*bmp1a* embryos (derived from homozygous M-*bmp1a* mutant females crossed to wild-type males), differing only in the ventral-most regions (Figures S3E, S3F, and S3I). This was also observed in M-*bmp1a*^{sa2416}/+ embryos (Figures S3G and S3J), supporting that the reduced P-Smad5 gradient is independent of the *bmp1a* mutation or strain background. *In situ* hybridization analysis revealed that *bmp1a* expression is diminished in both M-*bmp1a* and M-*bmp1a*/+ mutant embryos compared to controls (Figures S3K and S3L), which may explain the similarly reduced P-Smad5 gradients. We explored whether M-*bmp1a* is targeted for degradation by known mechanisms like miR-430 (Bazzini et al., 2012; Giraldez et al.,

2006), which could result in the aberrant degradation of wild-type *bmp1a* in M-*bmp1a*/+ embryos. However, based on existing RNA sequencing (Mishima and Tomari, 2016) and miR target scanning, *bmp1a* is not a target of miR-430, leaving the underlying mechanism to be determined.

M-*bmp1a* Embryos Rapidly Recover Peak BMP Signaling Levels

It was difficult to reconcile the early DV patterning defects in M-*bmp1a* mutant embryos (Figures 2J and 2J′) with their normal body plan (Figure 1D) unless BMP signaling and the P-Smad5 gradient recovered at a later stage. To investigate this, we quantified the P-Smad5 gradient 1.3 h later, at 7 hpf (mid-gastrulation). Accurate embryo staging was confirmed by relative nuclei density, which reveals clear landmark features that distinguish 5.3-, 5.7-, 6.3-, and 7-hpf embryos (Figure S4). At 7 hpf, both M-*bmp1a* and M-*bmp1a*^{sa2416}/+ embryos recovered peak ventral P-Smad5 levels and approached lateral wild-type levels at the margin (Figures 3A 3B, 3D, and S5A–S5F). More animally, M-*bmp1a*/+ embryos displayed a similar recovery pattern, while M-*bmp1a* embryos displayed a weaker recovery compared with the margin (Figures S5G–S5I). Overall, recovery of the P-Smad5 gradient in M-*bmp1a* embryos is consistent with previous studies that activated BMP signaling in embryos devoid of BMP signaling at 6 hpf (early gastrulation) and rescued the mutant phenotype (Tucker et al., 2008). In contrast, in embryos deficient for both M-Bmp1a and Tolloid, the P-Smad5 gradient remained effectively ablated embryo-wide (Figures 3C and 3D).

However, despite the recovery of peak P-Smad5 levels by 7 hpf, DV patterning defects in M-*bmp1a* and M-*bmp1a*/+ mutant embryos persisted. The cranial neurectoderm markers *otx2* and *gbx1* remained expanded at 8 hpf (Figures 3E, 3F, S5J, and S5K). This is consistent with previous studies showing that BMP signaling patterns anterior tissues such as the head earliest, between 4.7 and 6 hpf, compared to more caudal tissues (Bhat et al., 2013; Hashiguchi and Mullins, 2013; Tucker et al., 2008). Dorsal marker expansion may also persist because P-Smad5 levels in the lateral region (between 45° and 90°), though recovering, remain significantly below the wild type (Figures 3D and S5E). Thus, M-*bmp1a* mutants provide a powerful context to investigate the recovery of BMP signaling, the plasticity of the early gastrula, and how the embryo may compensate for an early expansion of neural tissues later during development.

Sizzled Is Dispensable for Early BMP Gradient Formation in Zebrafish

In M-*bmp1a* and M-*bmp1a/+* embryos, which exhibit significantly reduced P-Smad5 at 5.7 hpf (Figures 2H, 2I, and S3), we also observed reduced *sizzled* expression (Figure 4A). This is consistent with *sizzled* being induced by BMP signaling and Sizzled's role as a feedback inhibitor of Bmp1a/Tolloid (Collavin and Kirschner, 2003; Inomata et al., 2013; Lee et al., 2006; Martyn and Schulte-Merker, 2003; Yabe et al., 2003). *sizzled* mutants are mildly ventralized and, similar to *tolloid* mutants, this phenotype primarily affects the tail (Figure 1D) (Hammerschmidt et al., 1996). Although *sizzled* expression is responsive to BMP levels, we found that the P-Smad5 gradient in *sizzled* mutants remained unchanged in two null alleles (Figures 4B–4E). Since both *sizzled* and *tolloid* mutants displayed wild-type P-Smad5 gradients in the early gastrula (5.7 hpf) (Figures 2 and 4), and both mutants do not display DV patterning defects until mid- to late-gastrula stages (8–10 hpf) (Connors et al.,

1999, 2006; Hammerschmidt et al., 1996; Miller-Bertoglio et al., 1999), Sizzled and Tolloid likely shape the BMP gradient later in gastrulation to correctly pattern tail tissues.

Although Sizzled alone may not play a role in establishing the early BMP gradient, we postulated that Sizzled may contribute to the reduced P-Smad5 gradient in M-*bmp1a* and M-*bmp1a/+* embryos (Figures 2H, 2I, and S3). In M-Bmp1a-deficient embryos, Sizzled could be inhibiting Tolloid, which is still present, resulting in increased Chordin activity and a shallower P-Smad5 gradient. To directly test this, we quantified the P-Smad5 gradient in embryos deficient for both Bmp1a and Sizzled to determine if the additional loss of *sizzled* ameliorated the decreased M-*bmp1a/+* P-Smad5 gradient. However, we found no discernable difference between M-*bmp1a/+;sizzled* homozygotes and their M-*bmp1a/+* and M-*bmp1a/+;sizzled* heterozygous siblings (Figures 4F–4I). This indicates that Sizzled, on its own and in the sensitized M-*bmp1a/+* background, is dispensable for early BMP gradient formation in zebrafish, though this does not preclude an early role for Sizzled under other perturbations.

Expression Dynamics Likely Account for Distinct Requirements of Bmp1a/Tolloid Function

To incorporate Bmp1a and Tolloid into a mathematical model of BMP gradient formation, we determined the dynamics of *tolloid* gene expression in late blastula and early gastrula embryos using RNAscope. Previous *in situ* methods describing *tolloid* distribution in the early gastrula yielded limited spatial and temporal resolution due to intense puncta that dominated the chromogenic alkaline phosphatase signal (Connors et al., 1999). In contrast, RNAscope offers whole-mount fluorescence microscopy, enabling detection within individual nuclei and across distinct anteroposterior positions. Importantly, we found that *tolloid* expression is very low in the late blastula (4.7 hpf) but increases significantly in the early gastrula (5.7 hpf), and segmenting and extracting *tolloid* distribution at the margin revealed graded ventral-to-dorsal expression at 5.7 hpf (Figures 5A–5C and S6A). We also found that *tolloid* puncta correspond to nuclear transcripts (Figure S6A).

We used an updated mathematical model, described in the next section, to evaluate the roles of Tolloid and Bmp1a expression dynamics in BMP signaling gradient formation. We performed several computational screens (100,000 simulations each) with (1) varied distribution and onset of Tolloid and (2) ubiquitous Bmp1a either constant or degrading (Figure S6B; Tables S1 and S2). Graded Tolloid expression modestly increased the number of solutions that fit our measured P-Smad5 gradients compared to uniform Tolloid (Figure S6B, conditions 2 vs. 3 and 4 vs. 6). However, a later onset of Tolloid and constant Bmp1a expression resulted in the greatest number of solutions that fit our results (Figure S6B, conditions 2 vs. 6 and 3 vs. 4). These conditions (later Tolloid onset and constant Bmp1a) are consistent with our measurements of *tolloid* mRNA (Figures 5A–5C) and existing RNA sequencing that includes *bmp1a* during these stages (Mishima and Tomari, 2016). Furthermore, we identified the optimal Tolloid onset time to be 5.3 hpf (Figure S6C), supporting a less prominent role for Tolloid and its inability to substitute for loss of Bmp1a at 5.7 hpf (Figure 2). Taken together, temporal differences in Bmp1a and Tolloid expression may be key to their distinct roles in shaping the early BMP gradient.

Computational Screen Endorses Limited Chordin Range during BMP Gradient Formation

Our previous mathematical model of BMP gradient formation (Zinski et al., 2017) used a simplified model of Chordin proteolysis by a single metalloprotease, Tolloid, and did not consider Sizzled regulation. Since we found that Bmp1a plays an independent role in gradient formation (Figure 2), and Bmp1a and Tolloid display distinct expression patterns and dynamics (Figures 1B, 5A–5C, and S6A–S6C), we updated our mathematical model to separately describe Bmp1a and Tolloid processing of Chordin and their respective inhibition by Sizzled (Figure S6D). We also incorporated distinct Bmp1a and Tolloid expression patterns and dynamics: Bmp1a is uniformly high throughout, as it is maternally deposited, while Tolloid is graded with onset at 5.3 hpf (Figure 5D).

With this model, we performed multiple computational screens (100,000, 1 million, or 10 million simulations) of BMP gradient formation from 3.5 hpf, when wholesale zygotic transcription initiates, to 5.7 hpf, the early gastrula stage when we measured the P-Smad5 gradient. For each simulation, we solved a system of partial differential equations (Figure S6D) with a distinct combination of randomly varied values for unknown parameters. That same parameter combination was then re-simulated to predict the BMP signaling gradient in mutant conditions. Finally, simulated BMP signaling gradients were compared to respective measured P-Smad5 profiles for wild type; *chordin*, *sizzled*, *tolloid*, and M-*bmp1a* single mutants; and M-*bmp1a;tolloid* double mutants. Loss of *noggin* was compared to the wild-type P-Smad5 profile as an additional control (Zinski et al., 2017).

In iterative computational screens (I, II, and III, 1 million simulations each), the M-*bmp1a;tolloid* double- and M-*bmp1a* single-mutant P-Smad5 profiles were the most challenging to fit, consistently constraining the number of best-fit solutions (Tables S3 and S4). Increasing model fitness required adjusting the value ranges for three key parameters: Chordin diffusion (D_C) and BMP and Chordin production rates (ϕ_B and ϕ_C) (Figure S6E). Initially, D_C was fixed at 7 $\mu m^2/s$, the recently measured value in zebrafish (Pomreinke et al., 2017), but this generated zero solutions that simultaneously fit all mutant profiles (Table S4, screen I). Varying D_C up to 50 $\mu m^2/s$ markedly increased the number of solutions fitting the M-*bmp1a;tolloid* profile, but the M-*bmp1a* profile still had relatively few solutions, resulting in only one solution that fit all mutant profiles simultaneously (Table S4, screen II). In those M-*bmp1a* solutions, ϕ_B values were between 0.01 and 1 nM/s, at the lower end of its 0.01–100 nM/s (Zinski et al., 2017) range, and consistently less than ϕ_C. When we condensed the ϕ_B range to 0.01–1 nM/s and constrained ϕ_B to be less than ϕ_C, we doubled the number of solutions fitting the M-*bmp1a* profile and we were able to generate 16 solutions that fit all mutant profiles (Table S4, screen III). Based on the production rate values in these 16 solutions (Figure S6F), the range for ϕ_B was further lowered to 0.001–0.1 nM/s for our final screen.

Our final screen (10 million simulations) generated 182 model solutions that simultaneously fit all mutant P-Smad5 profiles within the experimentally observed error (Figure 5E; Tables S5 and S6). This is an impressive number of solutions, considering that the updated model increased both the number of mutant profiles each solution must fit (from 4 to 7) and the varied parameters (from 19 to 23, requiring a minimum of 2^{23} or ~8 million simulations

compared to 2^{19} or ~500,000 previously) (Zinski et al., 2017). From these 182 solutions, we found a minimum ϕ_C to ϕ_B ratio of 4.51 (Figure 5F), suggesting that BMP is produced at a significantly lower rate than Chordin in the embryo, consistent with relative protein estimations in *Xenopus* (Lee et al., 2006; Plouhinec et al., 2013). Even though D_C was varied up to 50 $\mu m^2/s$, the largest fraction of D_C values in our 182 solutions was consistent with the 7-$\mu m^2/s$ measurement by fluorescent recovery after photobleaching (FRAP) (Figure 5G) (Pomreinke et al., 2017). Higher D_C rates are also consistent with fluorescent correlation spectroscopy (FCS) measurements in both zebrafish (59 $\mu m^2/s$) and *Xenopus* (31 $\mu m^2/s$) (Inomata et al., 2013; Pomreinke et al., 2017).

Importantly, the final distributions of Chordin and BMP bound to Chordin (BMP-Chordin) in our 182 solutions can distinguish between the counter-gradient and source-sink mechanisms. In a counter-gradient, Chordin diffuses the length of the embryo, resulting in graded Chordin distribution across the DV axis (Figure 5H). Since long-range diffusion of Chordin predominates (Figure 1C), Chordin binds BMP close to the BMP source, resulting in a ventral peak of BMP-Chordin (Figure 5H). In contrast, in the source-sink model, the Chordin range re-mains limited dorsally to act as a sink (Figure 5H). Instead, since BMP diffusion predominates (Figure 1C), Chordin binds BMP distant from the BMP source, resulting in a dorsolateral (DL) peak of BMP-Chordin (Figure 5H). In all our 182 model solutions, the Chordin range is strictly restricted to the dorsal half of the embryo, with a DL peak of BMP-Chordin (Figure 5I). Therefore, based on our current experimental results, the modeling solutions predict a source-sink mechanism instead of the counter-gradient as a model of BMP gradient formation in the early zebrafish embryo.

Long-Range Chordin Diffusion Is Dispensable for DV Patterning

A defining feature of the source-sink mechanism is that Chordin is not required to diffuse to the ventral regions of the embryo (Figures 1C, 5H, and 5I); in fact, it must be prevented from doing so. Our findings implicate Bmp1a/Tolloid as the critical factors that restrict the Chordin range to generate a dorsal sink (Figure 2E). This mechanism predicts that dorsally restricted non-diffusible Chordin, in the absence of Bmp1a/Tolloid, is sufficient to generate a normal BMP gradient. We tested this prediction in our mathematical model by using non-diffusing Chordin (D_C=0) in a M-*bmp1a;tolloid*-deficient background (Table S7).

We performed 1 million simulations with varied immobile Chordin expression domains and found that many solutions (73,896) can generate a wild-type BMP gradient. We found that the majority (79.8%) of immobile Chordin domains in these solutions, which were varied in both size and location, were dorsally localized (Figures 6A and 6A′). These dorsal domains displayed mean lengths extending to 100° (180° is the dorsal midline) (Figures 6A and 6A′). This distribution of immobile Chordin in the dorsal half of the embryo is consistent with the Chordin distribution observed in the 182 screen solutions (Figure 5I). There were also many (19.7%) solutions with lateral domains, and the majority of these (89.1%) had a mean length that reached 100° as well (Figures 6A and 6A′). In contrast, there were very few (0.5%) solutions with ventral domains (Figures 6A and 6A′). Together, the individual and mean domain lengths of our modeling solutions suggest that non-diffusing Chordin would

primarily be required across DL regions and must reach 100°, near the halfway-point of the embryo (Figures 6A and 6A′).

To directly test whether long-range Chordin diffusion is required for DV patterning *in vivo*, we generated a membrane-tethered Chordin protein (Figure 6B). This construct has an N-terminal epitope tag and the rat integral-membrane protein, CD2, at the C terminus (HA-Chordin-CD2) (Ashe and Levine, 1999). Microinjection of *HA-chordin-CD2* mRNA in M-*bmp1a*/+ and wild-type embryos resulted in membrane localization, which was absent when the epitope-only control (*HA-chordin*) mRNA was injected (Figures 6C, 6D, and S7A). Notably, HA-Chordin-CD2 membrane localization was more clearly visible in M-*bmp1a*/+ than in wild-type embryos (Figures 6C and 6D), indicating that endogenous Bmp1a is very efficient at cleaving HA-Chordin-CD2 in wild-type embryos.

The N-terminal epitope tag does not affect Chordin activity (Figure S7B), and both HA-Chordin and HA-Chordin-CD2 were functional, dorsalizing embryos lacking endogenous Chordin, M-Bmp1a, and Tolloid (Figures 6E and 6F). Consistent with our earlier double-mutant analysis (Figure 1F), embryos deficient for M-Bmp1a and Tolloid, but wild-type or heterozygous for *chordin*, were severely dorsalized (Figures 6F, column 2, and 7A). In these embryos, ubiquitous expression of *HA-chordin* or *HA-chordin-CD2* mRNA had no adverse effects, even enhancing dorsalization (Figure 6F, columns 3 and 4). In contrast, *chordin* mutants also deficient for M-Bmp1a and Tolloid displayed the ventralized *chordin* mutant phenotype (Figures 6F, column 6, and 7A). This confirms that Bmp1a and Tolloid function exclusively through Chordin. Importantly, ubiquitous expression of *HA-chordin* or *HA-chordin-CD2* in *chordin* mutant embryos resulted in severe dorsalization (Figure 6F, columns 7 and 8). Thus, HA-Chordin-CD2, despite being localized to the membrane, fully inhibits BMP signaling embryo-wide in the absence of M-Bmp1a and Tolloid, like endogenous Chordin (Figure 6F, columns 8 vs 2).

Our computational modeling predicts that if Chordin acts as a sink rather than a counter-gradient (Figure 1C), then non-diffusible Chordin, in the absence of Bmp1a/Tolloid, should recapitulate a normal BMP signaling gradient if expressed dorsolaterally (Figures 6A and 6A′). To determine if localized immobile Chordin can correctly pattern the DV axis, we regionally expressed either epitope-only or membrane-tethered Chordin in embryos lacking endogenous Chordin, M-Bmp1a, and Tolloid (Figure 7A). We injected mRNAs for either construct and H3.3-mCherry (as the lineage tracer) into a single blastomere between the 8- and 16-cell stages (Figure 7B). This results in regionally limited expression since only cells descendant from the injected blastomere will express the construct and lineage tracer. Regional expression was determined by H3.3-mCherry fluorescence at 6.3 hpf, when the dorsal shield is apparent as a landmark. We consistently generated eight regions of expression (Figure 7B): regions limited to the ventral (V), lateral (lat), or dorsal (D) thirds of the embryo; ventrolateral (VL) or DL regions; regions spanning beyond the ventral (VB) or dorsal (DB) halves; and a region limited to the dorsal shield (sh), which recapitulates the *chordin* mRNA expression domain (Figure 1A′). The embryonic phenotype was evaluated at 13 hpf (8-somite stage) before identifying *chordin* mutants by genotyping.

M-*bmp1a;chordin* +/− and +/+ sibling controls were wild type, and injecting *tll1*MO resulted in radial dorsalization, confirming that *tll1*MO blocked Tolloid activity (Figure 7A). At 13 hpf, *chordin* mutants have a distinct ventralized phenotype, displaying reduced head and eyes and a thickening of posterior tissue (Hammerschmidt et al., 1996), which persist with or without M-Bmp1a/Tolloid (Figure 7A). Importantly, expression of HA-Chordin-CD2 in D, DL, and lat regions rescued these defects, indicating that it can recapitulate endogenous Chordin function (Figures 7C and 7D). In contrast, V expression of HA-Chordin-CD2 caused radial dorsalization, indicating that it blocks BMP activity (Figures 7C and 7D). Finally, restricted HA-Chordin-CD2 expression in the dorsal shield did not rescue *chordin* mutant ventralization, indicating that expression in this limited region is not sufficient (Figures 7C and 7D). These results are all consistent with our immobile Chordin modeling solutions, which predict that a rescuing region must extend to halfway across the embryo (Figures 6A and 6A′).

In contrast to HA-Chordin-CD2, expression of HA-Chordin in any region of an embryo deficient in Chordin, M-Bmp1a, and Tolloid resulted in radial dorsalization (Figure 7E). Since HA-Chordin is free to diffuse throughout the embryo without Bmp1a/Tolloid, it can block all BMP signaling regardless of expression region. This demonstrates that the ability of HA-Chordin-CD2 to rescue *chordin* mutant ventralization when expressed in DL regions is due to the presence of the CD2 membrane tether. Together, these data show that DL regional expression of immobile Chordin can pattern the DV axis, suggesting that embryo-wide Chordin diffusion in a counter-gradient is not required for BMP gradient formation. This supports our model that Bmp1a/Tolloid restrict the Chordin range to the dorsal half of the embryo, thus generating the sink that drives BMP gradient formation.

DISCUSSION

Here, we resolve the roles of the metalloproteases Bmp1a and Tolloid in BMP gradient formation. Our mutant analyses show that Tolloid is partially redundant to Bmp1a: both are required for DV patterning, but Bmp1a plays a non-redundant role in shaping the BMP gradient (Figures 1 and 2). Use of *bmp1a* mutants confirmed the epistatic relationship among Bmp1a, Tolloid, and Chordin (Figures 6 and 7), which is important because Bmp1a/Tolloid process additional substrates, such as procollagens (Hopkins et al., 2007), and a potential target was identified from the gene duplicate *chordin-like* (Branam et al., 2010). However, concomitant loss of Bmp1a, Tolloid, and Chordin resulted in a stereotypical *chordin* mutant phenotype (Figures 6 and 7), indicating that Chordin is the sole relevant substrate for Bmp1a and Tolloid proteolysis during gastrulation.

Implications from Quantitative Mutant P-Smad5 Analyses

Quantitation of the P-Smad5 gradient in *bmp1a*, *tolloid*, and *sizzled* single mutants provided exceptional spatial and temporal clarity. First, M-*bmp1a* embryos had a significantly diminished P-Smad5 gradient in the early gastrula that remarkably recovered by mid-gastrulation (Figures 2 and 3). This revealed an individual, albeit unexpected, role for Bmp1a in BMP gradient formation and early DV patterning. Additionally, given their wild-type 1-dpf appearance, M-*bmp1a* mutants present a biologically relevant context for future

studies into the mechanisms and patterning consequences of BMP gradient recovery. The similarities between M-*bmp1a* homozygous and heterozygous mutants (Figures S3 and S5) also warrant future investigation.

Second, both *tolloid* and *sizzled* single mutants, which have tail DV patterning defects, displayed normal P-Smad5 gradients at 5.7 hpf (Figures 2 and 4). This is consistent with previous studies describing later DV patterning defects in these mutants (Connors et al., 1999, 2006; Hammerschmidt et al., 1996; Miller-Bertoglio et al., 1999) and the model that more posterior tissues are progressively patterned later in development (Hashiguchi and Mullins, 2013; Tuazon and Mullins, 2015; Tucker et al., 2008). Future studies will have to address the roles of Tolloid and Sizzled during gastrulation. Since *sizzled* is expressed earlier (Figure 4), it may be translationally repressed to time its activity, similar to Lefty in the Nodal morphogen system (van Boxtel et al., 2015), though *sizzled* is not a miR-430 target based on our analysis of existing RNA sequencing (Mishima and Tomari, 2016). Additionally, as the embryo progresses through gastrulation, there is a rapid and dramatic reorganization of cells, which may affect BMP gradient shape and require specific regulators such as Tolloid and Sizzled (Connors et al., 2006; Tuazon and Mullins, 2015).

Mathematical Modeling with *In Vivo* Analysis: Bmp1a/Tolloid, the Keepers of a Chordin Sink

Combining our updated mathematical model of BMP gradient formation and RNAscope analysis (Figures 5 and S6), we identified and validated complexity in *tolloid* expression dynamics, which is non-uniform and likely first expressed as protein close to 5.3 hpf. This may account for our finding that Tolloid cannot compensate for the loss of Bmp1a, which is maternally deposited, during BMP signaling gradient formation (Figure 2). Iterative large-scale computational screens also revealed likely ranges, and even a relative ratio, for BMP and Chordin production rates, which are valuable for any future mathematical modeling in the field since these rates are difficult to measure *in vivo* (Figure 5).

Models with either diffusing or non-diffusing Chordin (Figures 5 and 6) support that regionally restricted Chordin is required to generate the BMP gradient. Despite likely being produced at almost 5-fold-higher rates than BMP and being highly diffusive (Figure 5) (Inomata et al., 2013; Pomreinke et al., 2017), Chordin distribution in our solutions remained restricted to the dorsal half of the embryo, inconsistent with the counter-gradient mechanism for BMP gradient formation in the early zebrafish embryo. The ability of Chordin to diffuse at long range is evident, however, in the absence of Bmp1a/Tolloid, when it can block all BMP signaling in the embryo (Figure 2). This further underscores Bmp1a/Tolloid as the keepers of a dorsal Chordin sink, essentially preventing an embryo-wide counter-gradient of Chordin from forming.

Our results that regional, non-diffusing Chordin can correctly pattern the embryo (Figure 7) provide pivotal *in vivo* support for the source-sink mechanism. Since a uniform, spatially limited region of Chordin can pattern the embryo, patterning information is not imparted by a long-range Chordin counter-gradient. Immobile Chordin rescuing regions extend through D, DL, and lat regions, consistent with our model results (Figures 5 and 6), and suggest an effective sink size. While some limited Chordin diffusion is likely required during normal

development to generate a correctly sized sink, embryo-wide Chordin diffusion is not the primary driving factor of BMP gradient formation. Instead, Chordin range must be restricted to the dorsal half of the embryo by Bmp1a/Tolloid, generating a dorsal sink.

While unlikely, it is possible our membrane-tethered Chordin fusion may exhibit yet-unknown protein expression dynamics, as was recently demonstrated in studies of membrane-tethered Wingless, the main *Drosophila* Wnt ligand (Alexandre et al., 2014; Chaudhary et al., 2019). We also cannot exclude that there may be very low levels of Chordin released from the membrane tether, as was postulated to occur in some *Drosophila* embryos (Ashe and Levine, 1999). To this end, future studies have the opportunity to further define the spatiotemporal characteristics of a Chordin sink through the development of light-inducible reagents to rapidly control timing and localization, and alternative approaches to immobilize Chordin.

Employing the Bmp1a/Tolloid Modality across Systems

The use of Bmp1a/Tolloid to limit Chordin range provides an exciting glimpse into how BMP can readily form a morphogen gradient in diverse biological contexts. For example, in contrast to zebrafish, BMP and Chordin homologs in *Drosophila* are expressed adjacent to each other, and the BMP gradient is generated by a counter-gradient of Chordin. This Chordin counter-gradient facilitates the diffusion of BMP back to its source, where Tolloid cleaves Chordin to release and concentrate BMP (O'Connor et al., 2006). Furthermore, in *Drosophila*, Tolloid only cleaves Chordin when it is bound to BMP (Marqués et al., 1997), demonstrating that the same components, which can be interchanged between organisms (Holley et al., 1995; Peluso et al., 2011), are dramatically repurposed in zebrafish to pattern the same axis through an entirely different mechanism. Thus, Bmp1a/Tolloid may represent a fundamental module of mechanistic flexibility, enabling the same signal (BMP) and antagonist (Chordin) to be employed across diverse environments of distinct shapes and sizes during development, homeostasis, or even disease.

STAR★METHODS

RESOURCE AVAILABILITY

Lead Contact—Further information and requests for resources and reagents should be directed to and will be fulfilled by the Lead Contact, Dr. Mary Mullins (mullins@pennmedicine.upenn.edu).

Materials Availability—Plasmids and zebrafish lines generated in this study are available upon request.

Data and Code Availability—MATLAB algorithms used for P-Smad5 gradient analysis have been previously published (Zinski et al., 2017, 2019).

Original segmented individual and mean P-Smad5 embryo data presented in all figures and supplements have been deposited to Mendeley Data: https://doi.org/10.17632/xtk7yyxt5f.1

Original MATLAB Code for the updated computational model of BMP gradient formation has been deposited to GitHub: https://github.com/xiaoweiwei20/FiniDiffModel-of-BMP-signaling-in-zebrafish

Parameter values for the 182 solution to our final 10 million simulation computational screen are listed in Table S6.

EXPERIMENTAL MODEL AND SUBJECT DETAILS

Zebrafish Adults and Embryos—Adult zebrafish were kept at 28° C in a 12-hr light/12-hr dark cycle. Most embryos used for experiments were between 0–14 hours post fertilization, with some phenotypes tracked from 1–5 days post fertilization. These were collected and raised at 28–31° C in E3 solution and grouped based on parental cross. In this study, sex/gender is not relevant since zebrafish sex determination takes place after 25 days post fertilization (Santos et al., 2017). The studies were performed in accordance with NIH guidelines and those of the University of Pennsylvania and were approved by the University of Pennsylvania IACUC.

Wild-type (TU)	RRID: ZIRC_ZL57
chordin^{tt250}	RRID: ZDB-ALT-980413-523, ZIRC_ZL61
tolloid^{tm124a}	RRID: ZDB-ALT-001220-2, ZIRC_ZL464
bmp1a^{t3116}	RRID: ZDB-ALT-061101-360, EZRC_9002
bmp1a^{sa2416}	RRID: ZDB-ALT-120411-333
sizzled^{rk1}	RRID: ZDB-ALT-030530-2
sizzled^{tm305}	RRID: ZDB-ALT-980203-1563, ZIRC_ZL830, EZRC_750

METHOD DETAILS

Genotyping—Genotyping of adults and embryos for the following alleles was performed using KASPar genotyping (Smith and Maughan, 2015). Primers were designed and generated by LGC Biosearch Technologies (previously KBioscience) to the following sequences flanking the [WT/mutant] nucleotide:

chordin^{tt250}	GTTTGGTGTGATGCACTGCGTTATGTGTCATTGTGAGCCG[G/A]
	TGAGTTGTGCACAGTTCAGTTTGAAATCCATATTGAATCT
tolloid^{tm124a}	TGGAGGAGTCATCCCTTACGTCATAGGAGGCAACTTCACC[G/T]
	GTAAGAGGACTAAGTGTTTGCCTTTTCAGCATCAATGTGT
bmp1a^{t31169}	GCACACGCGACCCGACAGAGACGAACACGTCAGTATCATA[C/T]
	GAGACAACATTCAGCCAGGTAGGAGAAAAAAACTGTAGGG
bmp1a^{sa2416}	CGAGAGGCATGATAACTGTGCGTACGACTACCTGGAGGTT[C/T]
	GAGACGGGAACTCRGAAAGCAGCCCGCTTTTGGGCAGGTT
sizzled^{rk1}	CCTTCGTCTGCTCGCTCATCGCCCCTGTATGCCTCGACAG[G/A]
	TACGTGTTGAGACACCTAAAATATTATGAGAAATACACAT

sizzled^{tm305} was genotyped as described in Yabe et al. (2003) by using the primer pair 5'-CCTCGATCTGACGACTTGAGGA-3' and 5'-GCCAGTTCTAAATCATGAGCTACAC-3'. The amplified PCR product was digested with *Taqα−1*, which cleaves the wild-type allele but not the mutant.

Bmp1a and Tolloid Comparison—Amino acid sequences of zebrafish Bmp1a and Tolloid were compared using LALIGN Pairwise Sequence Alignment (Chojnacki et al., 2017).

bmp1a Mutant Analysis—*bmp1a*^{t31169} fish were a gift from M. Harris. As reported, *bmp1a*^{t31169} homozygous females did not lay eggs (Bowen et al., 2012). Despite these females being gravid with mature oocytes, isolation of eggs for *in vitro* fertilization was also unsuccessful. However, by outcrossing *bmp1a*^{t31169} to the AB wild-type background, we were able to generate homozygous females that laid eggs over multiple generations.

Generating chordin^{tt250} Homozygotes—Adult viable *chordin*^{tt250} homozygous mutants were generated by injecting 300–600pg of *HA-chordin* mRNA into embryos from a heterozygous in-cross at the 1-cell stage. Embryos with a wild-type phenotype were raised and *chordin*^{tt250} homozygosity determined by genotyping the adults.

Embryo Pictures—All embryos were photographed using a Leica IC80HD camera at 12–48 hpf, as indicated. Brightness, contrast, and color balance were adjusted in the whole image in Photoshop.

In-Tube Controls For bmp1a Embryos—Since M-*bmp1a* embryos are generated by crossing a *bmp1a*$^{t31169/t31169}$ or *bmp1a*$^{sa2416/sa2416}$ female to a wild-type (TU) male, all progeny are M-*bmp1a* mutants. As such, there are no wild-type sibling controls for P-Smad5 and *in situ* DV marker analysis. The same is true for MZ-*bmp1a* mutants, whose siblings are M-*bmp1a*. To circumvent this, we added stage-matched wild-type embryos to the same Eppendorf tube as M- or MZ-*bmp1a* embryos prior to fixation and then fixed, stained, imaged, and processed both genotypes together. These in-tube wild-type controls (indicated by an asterisk in all figures) were identified by genotyping after imaging, ensuring that the M-*bmp1a* phenotype is not an artifact and analysis was blinded. In-tube controls were pooled with *tolloid/+* or *sizzled/+* sibling controls when appropriate.

In situ Hybridization for mRNA Domain Sizes—Whole-mount *in situ* hybridizations were performed using DIG-labeled anti-sense RNA probes (made with labeling kit: Roche 11277073910) to *pax2.1* (*pax2a*) (Krauss et al., 1992), *krox20* (Oxtoby and Jowett, 1993), *bmp1a* (Muraoka et al., 2006) and *sizzled* (Yabe et al., 2003) (gifts from M. Hibi), *chordin* (Miller-Bertoglio et al., 1997), *gata2* (Detrich et al., 1995), *foxb1a* (also known as *fkd3* and *foxb1.2*) (Odenthal and Nüsslein-Volhard, 1998), *otx2* (Li et al., 1994), and *gbx1* (Rhinn et al., 2003). Probes were visualized with anti-DIG-Alkaline Phosphatase (Roche 11093274910) developed with BM Purple (Roche 11442074001). Embryos were photographed using a Leica IC80HD either in PBS or cleared in BABB, a 1:2 ratio of benzyl alcohol (Sigma B-1042) and benzyl benzoate (Sigma B-6630). Images were processed using

ImageJ and animal view domain sizes determined by fitting a circle to each embryo and measuring the domain size angle at the circle center-point.

Fluorescent tolloid in situ Hybridization—Embryos were fixed with 4% PFA at room temperature for 4 hours, gradually dehydrated in methanol, and then incubated with Pretreat 3 (ACD #320045) at room temperature for 15 minutes to permeate the embryos. RNAscope probes *Chd-C1* (ACD #440081) and *Tld-C2* (ACD #475501-C2) were hybridized at 40 C for 16 hours. RNAscope Fluorescent multiplex detection reagents (ACD #320851) were used to stain the probes, specifically AltC was used for Amp4 in the staining kit, and DAPI was used to stain the nuclei.

Whole embryos were mounted with the animal region on the top and imaged with a 20×/1.0 Plan-Apochromat water immersion lens (D = 0.17 M27 75 mm). *tolloid* and *chordin* mRNA signals were imaged by 647nm and 555nm excitation wavelengths, respectively. XY pixels were 0.312 μm and Z pixels were 3 μm. The bottom 10% of each embryo (excluding the YSL) was extracted as the marginal layer and converted to a maximum projection image.

tolloid signal was segmented using a Gaussian filter to remove background and normalize each pixel from 0 to 1. All pixels above 0.08 and lower than 0.3 were extracted and the bwlabeln MATLAB function used to find all mRNA spots. The mRNA distribution was extracted by arranging each spot on a coordinate system. First, the center of the mRNA circle was moved to the (0,0) position in an x,y plane. Then, mRNA spot position was rotated based on the *chordin* expression, which defines dorsal. Finally, the mRNA spot number was calculated every 10 degrees and the two sides of the margin averaged to generate the ventral to dorsal profile of *tld* distribution.

Quantitative P-Smad5 Analysis—P-Smad5 immunostaining, imaging, and quantification were performed as described (Zinski et al., 2017, 2019). Briefly, embryos were fixed in 4% paraformaldehyde at 4°C, blocked in NCS-PBST, and probed overnight with a 1:100 dilution of anti-phosphoSmad1/5/8 antibody (Cell Signaling Technology Cat# 13820, RRID:AB_2493181), followed by a 1:500 dilution of goat anti-rabbit Alexa Fluor 647 (ThermoFisher Scientific Cat# A-21244, RRID:AB_141663) and a 1:2000 dilution of Sytox Green (ThermoFisher Scientific Cat# S7020). Embryos were cleared and mounted in BABB. Mounted embryos were imaged on a Zeiss LSM710 or LSM880 confocal microscope with an LD LCI Plan-Achromat 25X/0.8 lmm Corr DIC M27 multi-immersion lens in the oil-immersion setting. The same single bead from a calibration slide (ThermoFisher Scientific Cat#F369009, well A1) was imaged between embryos to account for any fluctuations in laser power.

Post-acquisition P-Smad5 analysis utilized a custom MATLAB algorithm to identify individual nuclei center-points and extract P-Smad5 intensities in each nucleus (Zinski et al., 2017, 2019), which were normalized based on a standard calibration bead intensity. Resulting embryos were aligned across the DV axis and conformed using Coherent Point Drift. Population means were generated after genotyping for in-tube/heterozygous sibling controls since all imaging and analysis was performed blinded. Mean profiles were generated by averaging P-Smad5 intensities of cells in a 30μm band either at the margin or

more animal positions. 3-D embryo-wide displays of mean P-Smad5 were generated by projecting all nuclei on a sphere divided into 4800 equilateral triangles and nuclei within each triangle averaged together. Nuclei density was similarly displayed, with a heatmap depicting nuclei number within each triangle relative to the total number of nuclei. We confirmed that the nuclei density of each individual embryo matched the qualitative features of the stage being investigated, detailed in Figure S4. The option to display either mean P-Smad5 intensity or relative nuclei density resides in the 'icosdisplay' function.

Generating Immobile Chordin—Membrane-tethered Chordin was generated by by inserting the rat *CD2* cDNA fragment from the *sog-CD2* construct (a gift from H. Ashe) used for similar experiments in *Drosophila* (Ashe and Levine, 1999). The *CD2* fragment (which lacks the signal sequence) was amplified by PCR with an additional N-terminal *ClaI* site and inserted in-frame at the *ClaI* site in zebrafish *chordin*-PCS2, which is upstream of the *stop* codon. An N-terminal HA epitope tag was also inserted downstream of the *chordin* signal sequence.

Embryo Microinjection—Embryos were injected with 2–3ng of *tll1* MO1 (GCAGAGTAAAGGTAGTCCATCTGAG) at the 1-cell stage. mRNA for *HA-Chordin* and *HA-Chordin-CD2* were generated using the SP6 MMessage Machine kit (ThermoFisher Science AM1340) and *H3.3-mCherry* mRNA (Smoak et al., 2016) was a gift from A. Jamieson-Lucy. 800pg of *HA-Chordin* and *HA-Chordin-CD2* were injected at the 1-cell stage for HA-immunostaining and localization analysis, described below. For regional expression, 250–450 pg of *HA-Chordin-CD2* with 500 pg of *H3.3-mCherry* was injected into a single blastomere at the 8- to 16-cell stage (total injection volume was no more than 0.5 nl). This is within the same range that rescued *chordin* mutants (described in Generating chordin^{tt250} Homozygotes section above).

HA Immunostaining and Imaging—Embryos injected with 800pg of *HA-Chordin* or *HA-Chordin-CD2* at the 1-cell stage were fixed in 4% paraformaldehyde at 4°C, blocked in NCS-PBST, and probed overnight with a 1:500 dilution of rabbit anti-HA (Thermo Fisher Scientific Cat# 71–5500, RRID:AB_2533988) and 1:1000 dilution of mouse anti-β-catenin (BD Biosciences Cat# 610153, RRID:AB_397554). This was followed by incubation in a 1:500 dilution of goat anti-rabbit Alexa Fluor 594 (Thermo Fisher Scientific Cat# A-11037, RRID:AB_2534095), a 1:500 dilution of goat anti-mouse Alexa Fluor 633 (Thermo Fisher Scientific Cat# A-21126, RRID:AB_2535768), and a 1:2000 dilution of Sytox Green (ThermoFisher Scientific Cat# S7020). Embryos were imaged on a Zeiss LSM880 confocal microscope with a C-Apochromat 40X/1.2 NA W Corr objective. Colocalization of HA and β-catenin immunofluorescence was performed using the ImarisColoc module on Imaris 9.5.1. Intensity thresholds were determined by the un-injected controls and then applied to the entire dataset.

Bubble Plots—Bubble plots categorizing embryo phenotypes (Figures 6F, 7D, 7E, and S7B–S7D) were generated in Microsoft Excel. Bubble, or circle, size was determined by the ratio of the number of embryos the circle represents and the total number of embryos in that

genotype for each experiment. This size is displayed as the area of the circle. Exact values of n and number of replicates can be found in the figure legends.

Regional Expression Domain Classification—After single blastomere injections, the expression regions of *HA-chordin* and *HA-chordin-CD2* were determined by H3.3-mCherry fluorescence under a fluorescent dissecting microscope. This was performed at 6.3 hpf, when the dorsal shield is most prominent and acts as a landmark designating dorsal. The vast majority of embryos could be classified into eight distinct regions of expression (Figure 7B), defined as follows: ventral (V) and dorsal (D) regions occupy their respective third of the embryo; ventrolateral (VL) regions span anywhere from 0–100° and dorsolateral (DL) regions span anywhere from 80–180°; ventral broad (VB) and dorsal broad (DB) regions extend beyond their respective half (90°) of the embryo; lateral (lat) regions span between 45–135°; and shield (sh) regions are limited to the dorsal shield.

Embryos with no visible H3.3-mCherry fluorescence were added to the *tll1*MO-only control group. Embryos with ubiquitous H3.3-mCherry fluorescence were added to the 1-cell injection analysis (Figure 6F) for the appropriate construct. The very few embryos with unclassifiable expression or disrupted morphology were removed from analysis.

Mathematical Modeling

Reaction-Diffusion Equations

$$\frac{\partial B}{\partial t} = D_B\frac{\partial^2 B}{\partial x^2} + \phi_B(x) + \lambda_{tBC}\cdot\frac{1}{1+S/kit+(C+BC)/kmt}\cdot BC + \lambda_{aBC} \cdot\frac{1}{1+S/kia+(C+BC)/kma}\cdot BC \cdot - k_{onC}B\cdot C - k_{offC}BC - k_{onN}B\cdot N + k_{offN}BN - dec_B B \quad (1)$$

$$\frac{\partial C}{\partial t} = D_C\frac{\partial^2 C}{\partial x^2} + \phi_C(x) - \lambda_{tC}\cdot\frac{1}{1+S/kit+(C+BC)/kmt}\cdot C - \lambda_{aC} \cdot\frac{1}{1+S/kia+(C+BC)/kma}\cdot C - k_{onC}B\cdot C - k_{offC}BC - dec_C C \quad (2)$$

$$\frac{\partial N}{\partial t} = D_N\frac{\partial^2 N}{\partial x^2} + \phi_N(x) - k_{onN}B\cdot N + k_{otfV}BN - dec_N N \quad (3)$$

$$\frac{\partial BC}{\partial t} = D_{BC}\frac{\partial^2 BC}{\partial x^2} - \lambda_{tBC}\cdot\frac{1}{1+S/kit+(C+BC)/kmt}\cdot BC \cdot - \lambda_{aBC} \cdot\frac{1}{1+S/kia+(C+BC)/kma}\cdot BC + k_{onC}B\cdot C - k_{offC}BC - dec_{BC}BC \quad (4)$$

$$\frac{\partial BN}{\partial t} = D_{BN}\frac{\partial^2 BN}{\partial x^2} + k_{onN}B \cdot N - k_{offN}BN - dec_{BN}BN \quad 5)$$

$$\frac{\partial S}{\partial t} = D_S\frac{\partial^2 S}{\partial x^2} + \frac{Vs \cdot B^n}{k^n + B^n} - dec_s S \quad 6)$$

$$\frac{etaS}{Vs} = \frac{p * b^n}{\frac{k^n}{B0} + b^n} \quad 7)$$

The system of partial differential equations (PDE) listed above, and in Figure S6D, describes zebrafish development from blastula to early gastrula stages (3.5 hpf to 5.7 hpf). BMP ligand, Chordin, Noggin and Sizzled are denoted by *B*, *C*, *N* and *S*, and the complexes of BMP-Chordin and BMP-Noggin are denoted by *BC* and *BN*, respectively. Notably, while our previous mathematical model (Zinski et al., 2017) used a simple linear proteolysis model of Chordin by Tolloid alone, this updated model explicitly uses enzyme saturation kinetics to model Chordin proteolysis by Tolloid or Bmp1a separately and the distinct competitive inhibition of Tolloid or Bmp1a by Sizzled.

The embryo is divided into 36 nodes from ventral (x=0) to dorsal (x=700μm). PDE were solved as before (Zinski et al., 2017), with either 100,000, 1 million, or 10 million groups of known and randomly varied parameters (Tables S1, S3, S5, and S7) and proteins symmetrically distributed. For each parameter matrix, the model was solved in wild-type and 6 loss of function conditions: for *chordin, noggin,* and *sizzled* loss of function, the production rate was set to zero; for M-*bmp1a* and *tolloid* single mutants and M-*bmp1a;tolloid* double mutants, the λ (maximum degradation velocity) of the corresponding protein was set to zero. The normalized root-mean-square deviation (NRMSD) between each model and the corresponding P-Smad5 profile was calculated to find the best fit models (see Quantification and Statistical Analysis section for more detail).

Model Input—Production regions of BMP, Chordin and Noggin (Figure 5D) were previously determined (Zinski et al., 2017). Production rates (ϕ) of BMP, Chordin and Noggin are not known and were screened as varied parameters Chordin and BMP decay rates and BMP diffusion were fixed based on recent measurements (Pomreinke et al., 2017; Zinski et al., 2017).

The production region of Tolloid was determined by RNAscope (Figures 5A–5C) and Bmp1a by alkaline phosphatase *in situ* (Figure 1B). Optimal Tolloid and Bmp1a dynamic expression (Figure 1D) was determined by expression screens, described in the next section. The λ term represents the maximum degradation velocity of Chordin or BMP-Chordin by the proteinase Tolloid (λ_t) or Bmp1a (λ_a), as indicated. These, as well as the Michaelis constants of Tolloid (*kmt*) and Bmp1a (*kma*), were screened as varied parameters.

Since *sizzled* expression is induced by BMP signaling (Figure 4A) (Yabe et al., 2003), we estimated Sizzled expression based on BMP signaling levels using a gene control feedback term. Sizzled was considered a target of BMP signaling that could be described by the Hill equation (the second term in Equation 6), which was transformed to Equation 7 to compress parameters. *etaS* represents the production of Sizzled and *Vs* is the maximum of Sizzled expression, so *etaS*/*Vs* (Equation 7) describes the shape of Sizzled expression from ventral to dorsal. B0 is the maximum of BMP and *b* is B/B0, which can be described by the pSmad distribution. Following the Hill equation, *p* is the scaled parameter, *K* is concentration of BMP at half-maximum, and *n* is the gene-control cooperativity parameter.

To determine the fixed values of *p*, *n*, and K/B0 we measured the distribution of *sizzled* mRNA (*etaS*/*Vs*) and compared it directly to the stage-matched distribution of P-Smad5 (*b*). Interestingly, the *sizzled* expression profile is narrower overall than the P-Smad5 profile, which presumably drives *sizzled* expression. Using the Lsqnonlin nonlinear data-fitting function in MATLAB, we fit the distributions:

$$\frac{etaS}{Vs} = exp(-(x-23.19)/50)/(0.02+exp(-(x-23.19)/50))$$

$$b = \exp(-(x-1828000)/714400)/(0.2+\exp((x-427.7)/61.26))$$

Combining these expressions in Equation 7, we solved for *p* (=164), *n* (=4), and K/B0, which became fixed values in all of our simulations as we calculate saturation and production kinetics. A previous model of Sizzled in zebrafish used an *n* value of 20 (Pomreinke et al., 2017), which is essentially a switch-like behavior. This would theoretically require 20 P-Smad5 binding sites on the *sizzled* promoter, while our analysis of the putative regulatory region suggests only 4 binding sites, which are TTGTCTGCGAC, ATCTCTGTCTT, CACACAGACAC and CCAACAGACAT (Farré et al., 2003; Messeguer et al., 2002).

Cooperative Parameter/Hill Coefficient	*n*	4
Scaled Parameter	*p*	164
K/B0		4.1

Initially, we generated B0 in 1 million parameter simulations. We ran the model with only BMP, Chordin and Noggin and B0 was the maximum of BMP in Chd-/−. These B0 values were used to determine Sizzled expression and the *ki* range. *ki* is the dissociation constant of Tolloid (*kit*) or Bmp1a (*kia*) with Sizzled, which is described as a competitive inhibitor (Lee et al., 2006). To determine the *ki* range for our parameter screen, we calculated the maximum of Sizzled based on B0 and the corresponding *ki* was assigned a random value between 1/10 and 10 times the maximum of Sizzled.

Bmp1a and Tolloid Expression Dynamics Screens—The inputs and expression dynamics conditions tested are listed in Tables S1 and S2. For each group, we ran 100,000

simulations as described above, though BN and BC decay terms (Equations 4 and 5) were not included. The number of solutions that fit measured WT, M-*bmp1a* and *tolloid* single mutant, and M-*bmp1a;tolloid* double mutant P-Smad5 profiles (NRMSD <0.12) was compared to determine the optimal combination of expression conditions (Figure S6B; Table S2). To determine the optimal onset time of Tolloid expression, we ran eleven screens (100,000 simulations each) with the onset time for each screen set at distinct 12-minute intervals (Figure S6C). Again, the number of solutions that fit measured WT, M-*bmp1a* and *tolloid* single mutant, and M-*bmp1a;tolloid* double mutant P-Smad5 profiles (NRMSD<0.12) was compared to determine the optimal onset time (Figure S6C).

Large-Scale Screens—After determining optimal Bmp1a/Tolloid input conditions (Figure 5D), as described above, we performed three (I, II, III) screens of 1 million simulations each with the inputs listed in Table S3. Initially, when we fixed D_C at the published value of 7 $\mu m^2/s$ (Pomreinke et al., 2017), there were no solutions that adequately fit all our mutant profiles (Table S4, screen I). When we varied D_C up to 50 $\mu m^2/s$ we almost tripled the number of solutions fitting the M-*bmp1a;tolloid* profile, but M-*bmp1a* remained constraining (Table S4, screen II). In these solutions we found that production rates ϕ_B and ϕ_C were restricted to much lower ranges (0.01–1 nM/s and 0.1–10 nM/s, respectively) and ϕ_B was consistently less than ϕ_C. By repeating the model under these conditions, we doubled the number of M-*bmp1a* fitting solutions and were able to generate 16 solutions (NRMSD<0.11 for wt, *tolloid*, *chordin*, and *sizzled*; <0.06 for M-*bmp1a* and M-*bmp1a;tolloid*) (Table S4, screen III).

Our final screen consisted of 10 million simulations to adequately sample the parameter space since 2^{23} (the number of varied parameters) requires a minimum of ~8 million simulations. Inputs are listed in Table S5 and largely follow the conditions of screen III (Table S3), with the exception that ϕ_B and ϕ_C were further lowered to 0.001–0.1 nM/s and 0.01–10 nM/s, respectively, based on the production values of the 16 solutions from screen III (Figure S6F). We found 182 solutions (NRMSD<0.11 for wt, *tolloid*, *chordin*, and *sizzled*, as before; and lowered to <0.05 for M-*bmp1a* and M-*bmp1a;tolloid*), with the parameters for each solution listed in Table S6 and results displayed in Figures 5E–5G and 5I.

Immobile Chordin Simulations—1 million simulations were performed with immobile Chordin ($D_C = 0$) in a M-*bmp1a;tolloid* double mutant background (λ_t=0, λ_a=0) and the initial and final positions the immobile Chordin domain varied by 5° intervals from 0–180°, or ~19 μm intervals from 0–700 μm (Table S7). All other parameters remained identical to those of the final 10 million simulation screen (Table S5). Solutions were fit with the wild-type P-Smad5 profiles (NRMSD < 0.08), giving 73,896 total solutions. Solutions were classified in Figures 6A and 6A′ as dorsal, lateral, or ventral based on the dorsal-most site of the region: ventral as 0–60°, lateral as 60–120°, and dorsal as 120–180°.

QUANTIFICATION AND STATISTICAL ANALYSIS

All measurements or embryo classification were performed blinded, with embryos genotyped and grouped after.

Exact values of n (number of embryos) and number of replicates (defined as clutches from separate pairs of parents) can be found in the figure legends.

To determine if two P-Smad5 profiles were significantly different, two-tailed T-Tests were performed with a 5% significance level.

Profiles shown represent the mean with errors bars indicating standard deviation.

To determine if domain sizes of DV markers were significantly different, two-tailed T-Tests were performed with a 5% significance level on angle measurements using Prism8 (GraphPad).

Best-fit model solutions were determined by normalized root-mean-square deviation (NRMSD) error thresholds. Relative threshold NRMSD values were calculated based on the standard deviation observed in each P-Smad5 profile.

Supplementary Material

Refer to Web version on PubMed Central for supplementary material.

ACKNOWLEDGEMENTS

We thank the UPenn CDB Microscopy Core, especially A. Stout; H. Ashe for the *sog-CD2* construct; M. Hibi for the *bmp1a* and *sizzled* probe constructs; A. Jamieson-Lucy for the *H3.3* mRNA and figure consultation; M. Harris for *bmp1a*^{t31169} fish; J. Zinski for consultation; undergraduate students J. Aykit and R. Fernandez for genotyping; and past and present members of the Mullins lab for invaluable contributions. This work was supported by NIH funding: T32-GM007229 and F31-GM113362 (F.B.T.), R01-GM056326 and R35-GM131908 (M.C.M.), and R01-HD073156 (D.U. and M.C.M.).

REFERENCES

Agathon A, Thisse C, and Thisse B (2003). The molecular nature of the zebrafish tail organizer. Nature 424, 448–452. [PubMed: 12879074]

Alexandre C, Baena-Lopez A, and Vincent JP (2014). Patterning and growth control by membrane-tethered Wingless. Nature 505, 180–185. [PubMed: 24390349]

Asharani PV, Keupp K, Semler O, Wang W, Li Y, Thiele H, Yigit G, Pohl E, Becker J, Frommolt P, et al. (2012). Attenuated BMP1 function compromises osteogenesis, leading to bone fragility in humans and zebrafish. Am. J. Hum. Genet 90, 661–674. [PubMed: 22482805]

Ashe HL, and Briscoe J (2006). The interpretation of morphogen gradients. Development 133, 385–394. [PubMed: 16410409]

Ashe HL, and Levine M (1999). Local inhibition and long-range enhancement of Dpp signal transduction by Sog. Nature 398, 427–431. [PubMed: 10201373]

Bazzini AA, Lee MT, and Giraldez AJ (2012). Ribosome profiling shows that miR-430 reduces translation before causing mRNA decay in zebrafish. Science 336, 233–237. [PubMed: 22422859]

Bhat N, Kwon HJ, and Riley BB (2013). A gene network that coordinates preplacodal competence and neural crest specification in zebrafish. Dev. Biol 373, 107–117. [PubMed: 23078916]

Bier E, and De Robertis EM (2015). EMBRYO DEVELOPMENT. BMP gradients: A paradigm for morphogen-mediated developmental patterning. Science 348, aaa5838. [PubMed: 26113727]

Blader P, Rastegar S, Fischer N, and Strähle U (1997). Cleavage of the BMP-4 antagonist chordin by zebrafish tolloid. Science 278, 1937–1940. [PubMed: 9395394]

Bowen ME, Henke K, Siegfried KR, Warman ML, and Harris MP (2012). Efficient mapping and cloning of mutations in zebrafish by low-coverage whole-genome sequencing. Genetics 190, 1017–1024. [PubMed: 22174069]

Branam AM, Hoffman GG, Pelegri F, and Greenspan DS (2010). Zebrafish chordin-like and chordin are functionally redundant in regulating patterning of the dorsoventral axis. Dev. Biol 341, 444–458. [PubMed: 20226780]

Briscoe J, and Small S (2015). Morphogen rules: design principles of gradient-mediated embryo patterning. Development 142, 3996–4009. [PubMed: 26628090]

Chaudhary V, Hingole S, Frei J, Port F, Strutt D, and Boutros M (2019). Robust Wnt signaling is maintained by a Wg protein gradient and Fz2 receptor activity in the developing Drosophila wing. Development 146, dev174789. [PubMed: 31399474]

Chojnacki S, Cowley A, Lee J, Foix A, and Lopez R (2017). Programmatic access to bioinformatics tools from EMBL-EBI update: 2017. Nucleic Acids Res. 45, W550–W553. [PubMed: 28431173]

Collavin L, and Kirschner MW (2003). The secreted Frizzled-related protein Sizzled functions as a negative feedback regulator of extreme ventral mesoderm. Development 130, 805–816. [PubMed: 12506010]

Connors SA, Trout J, Ekker M, and Mullins MC (1999). The role of tolloid/mini fin in dorsoventral pattern formation of the zebrafish embryo. Development 126, 3119–3130. [PubMed: 10375503]

Connors SA, Tucker JA, and Mullins MC (2006). Temporal and spatial action of tolloid (mini fin) and chordin to pattern tail tissues. Dev. Biol 293, 191–202. [PubMed: 16530746]

De Robertis EM, and Moriyama Y (2016). The Chordin Morphogenetic Pathway. Curr. Top. Dev. Biol 116, 231–245. [PubMed: 26970622]

Detrich HW 3rd, Kieran MW, Chan FY, Barone LM, Yee K, Rundstadler JA, Pratt S, Ransom D, and Zon LI (1995). Intraembryonic hematopoietic cell migration during vertebrate development. Proc. Natl. Acad. Sci. USA 92, 10713–10717. [PubMed: 7479870]

Dutko JA, and Mullins MC (2011). SnapShot: BMP signaling in development. Cell 145, 636, 636.e1–636.e2. [PubMed: 21565618]

Farré D, Roset R, Huerta M, Adsuara JE, Roselló L, Albà MM, and Messeguer X (2003). Identification of patterns in biological sequences at the ALGGEN server: PROMO and MALGEN. Nucleic Acids Res. 31, 3651–3653. [PubMed: 12824386]

Giraldez AJ, Mishima Y, Rihel J, Grocock RJ, Van Dongen S, Inoue K, Enright AJ, and Schier AF (2006). Zebrafish MiR-430 promotes deadenylation and clearance of maternal mRNAs. Science 312, 75–79. [PubMed: 16484454]

Gistelinck C, Kwon RY, Malfait F, Symoens S, Harris MP, Henke K, Hawkins MB, Fisher S, Sips P, Guillemyn B, et al. (2018). Zebrafish type I collagen mutants faithfully recapitulate human type I collagenopathies. Proc. Natl. Acad. Sci. USA 115, E8037–E8046. [PubMed: 30082390]

Hammerschmidt M, Pelegri F, Mullins MC, Kane DA, van Eeden FJ, Granato M, Brand M, Furutani-Seiki M, Haffter P, Heisenberg CP, et al. (1996). dino and mercedes, two genes regulating dorsal development in the zebrafish embryo. Development 123, 95–102. [PubMed: 9007232]

Hashiguchi M, and Mullins MC (2013). Anteroposterior and dorsoventral patterning are coordinated by an identical patterning clock. Development 140, 1970–1980. [PubMed: 23536566]

Heasman J (2006). Patterning the early Xenopus embryo. Development 133, 1205–1217. [PubMed: 16527985]

Hild M, Dick A, Rauch GJ, Meier A, Bouwmeester T, Haffter P, and Hammerschmidt M (1999). The smad5 mutation somitabun blocks Bmp2b signaling during early dorsoventral patterning of the zebrafish embryo. Development 126, 2149–2159. [PubMed: 10207140]

Holley SA, Jackson PD, Sasai Y, Lu B, De Robertis EM, Hoffmann FM, and Ferguson EL (1995). A conserved system for dorsal-ventral patterning in insects and vertebrates involving sog and chordin. Nature 376, 249–253. [PubMed: 7617035]

Hopkins DR, Keles S, and Greenspan DS (2007). The bone morphogenetic protein 1/Tolloid-like metalloproteinases. Matrix Biol. 26, 508–523. [PubMed: 17560775]

Hur M, Gistelinck CA, Huber P, Lee J, Thompson MH, Monstad-Rios AT, Watson CJ, McMenamin SK, Willaert A, Parichy DM, et al. (2017). MicroCT-based phenomics in the zebrafish skeleton reveals virtues of deep phenotyping in a distributed organ system. eLife 6, e26014. [PubMed: 28884682]

Inomata H, Shibata T, Haraguchi T, and Sasai Y (2013). Scaling of dorsal-ventral patterning by embryo size-dependent degradation of Spemann's organizer signals. Cell 153, 1296–1311. [PubMed: 23746842]

Jasuja R, Voss N, Ge G, Hoffman GG, Lyman-Gingerich J, Pelegri F, and Greenspan DS (2006). bmp1 and mini fin are functionally redundant in regulating formation of the zebrafish dorsoventral axis. Mech. Dev 123, 548–558. [PubMed: 16824737]

Jasuja R, Ge G, Voss NG, Lyman-Gingerich J, Branam AM, Pelegri FJ, and Greenspan DS (2007). Bone morphogenetic protein 1 prodomain specifically binds and regulates signaling by bone morphogenetic proteins 2 and 4. J. Biol. Chem 282, 9053–9062. [PubMed: 17255107]

Kettleborough RN, Busch-Nentwich EM, Harvey SA, Dooley CM, de Bruijn E, van Eeden F, Sealy I, White RJ, Herd C, Nijman IJ, et al. (2013). A systematic genome-wide analysis of zebrafish protein-coding gene function. Nature 496, 494–497. [PubMed: 23594742]

Kok FO, Shin M, Ni CW, Gupta A, Grosse AS, van Impel A, Kirchmaier BC, Peterson-Maduro J, Kourkoulis G, Male I, et al. (2015). Reverse genetic screening reveals poor correlation between morpholino-induced and mutant phenotypes in zebrafish. Dev. Cell 32, 97–108. [PubMed: 25533206]

Krauss S, Maden M, Holder N, and Wilson SW (1992). Zebrafish pax[b] is involved in the formation of the midbrain-hindbrain boundary. Nature 360, 87–89. [PubMed: 1436081]

Lee HX, Ambrosio AL, Reversade B, and De Robertis EM (2006). Embryonic dorsal-ventral signaling: secreted frizzled-related proteins as inhibitors of tolloid proteinases. Cell 124, 147–159. [PubMed: 16413488]

Lele Z, Bakkers J, and Hammerschmidt M (2001). Morpholino phenocopies of the swirl, snailhouse, somitabun, minifin, silberblick, and pipetail mutations. Genesis 30, 190–194. [PubMed: 11477706]

Li Y, Allende ML, Finkelstein R, and Weinberg ES (1994). Expression of two zebrafish orthodenticle-related genes in the embryonic brain. Mech. Dev 48, 229–244. [PubMed: 7893604]

Little SC, and Mullins MC (2006). Extracellular modulation of BMP activity in patterning the dorsoventral axis. Birth Defects Res. C Embryo Today 78, 224–242. [PubMed: 17061292]

Marqués G, Musacchio M, Shimell MJ, Wünnenberg-Stapleton K, Cho KW, and O'Connor MB (1997). Production of a DPP activity gradient in the early Drosophila embryo through the opposing actions of the SOG and TLD proteins. Cell 91, 417–426. [PubMed: 9363950]

Martyn U, and Schulte-Merker S (2003). The ventralized ogon mutant phenotype is caused by a mutation in the zebrafish homologue of Sizzled, a secreted Frizzled-related protein. Dev. Biol 260, 58–67. [PubMed: 12885555]

Massagué J, Seoane J, and Wotton D (2005). Smad transcription factors. Genes Dev. 19, 2783–2810. [PubMed: 16322555]

Messeguer X, Escudero R, Farré D, Núñez O, Martínez J, and Albà MM (2002). PROMO: detection of known transcription regulatory elements using species-tailored searches. Bioinformatics 18, 333–334. [PubMed: 11847087]

Miller-Bertoglio VE, Fisher S, Sánchez A, Mullins MC, and Halpern ME (1997). Differential regulation of chordin expression domains in mutant zebrafish. Dev. Biol 192, 537–550. [PubMed: 9441687]

Miller-Bertoglio V, Carmany-Rampey A, Fürthauer M, Gonzalez EM, Thisse C, Thisse B, Halpern ME, and Solnica-Krezel L (1999). Maternal and zygotic activity of the zebrafish ogon locus antagonizes BMP signaling. Dev. Biol 214, 72–86. [PubMed: 10491258]

Mishima Y, and Tomari Y (2016). Codon Usage and 3′ UTR Length Determine Maternal mRNA Stability in Zebrafish. Mol. Cell 61, 874–885. [PubMed: 26990990]

Mullins MC, Hammerschmidt M, Kane DA, Odenthal J, Brand M, van Eeden FJ, Furutani-Seiki M, Granato M, Haffter P, Heisenberg CP, et al. (1996). Genes establishing dorsoventral pattern formation in the zebrafish embryo: the ventral specifying genes. Development 123, 81–93. [PubMed: 9007231]

Muraoka O, Shimizu T, Yabe T, Nojima H, Bae YK, Hashimoto H, and Hibi M (2006). Sizzled controls dorso-ventral polarity by repressing cleavage of the Chordin protein. Nat. Cell Biol 8, 329–338. [PubMed: 16518392]

O'Connor MB, Umulis D, Othmer HG, and Blair SS (2006). Shaping BMP morphogen gradients in the Drosophila embryo and pupal wing. Development 133, 183–193. [PubMed: 16368928]

Odenthal J, and Nüsslein-Volhard C (1998). fork head domain genes in zebrafish. Dev. Genes Evol 208, 245–258. [PubMed: 9683740]

Oxtoby E, and Jowett T (1993). Cloning of the zebrafish krox-20 gene (krx-20) and its expression during hindbrain development. Nucleic Acids Res. 21, 1087–1095. [PubMed: 8464695]

Peluso CE, Umulis D, Kim YJ, O'Connor MB, and Serpe M (2011). Shaping BMP morphogen gradients through enzyme-substrate interactions. Dev. Cell 21, 375–383. [PubMed: 21839924]

Piccolo S, Sasai Y, Lu B, and De Robertis EM (1996). Dorsoventral patterning in Xenopus: inhibition of ventral signals by direct binding of chordin to BMP-4. Cell 86, 589–598. [PubMed: 8752213]

Piccolo S, Agius E, Lu B, Goodman S, Dale L, and De Robertis EM (1997). Cleavage of Chordin by Xolloid metalloprotease suggests a role for proteolytic processing in the regulation of Spemann organizer activity. Cell 91, 407–416. [PubMed: 9363949]

Plouhinec JL, Zakin L, Moriyama Y, and De Robertis EM (2013). Chordin forms a self-organizing morphogen gradient in the extracellular space between ectoderm and mesoderm in the Xenopus embryo. Proc. Natl. Acad. Sci. USA 110, 20372–20379. [PubMed: 24284174]

Pomreinke AP, Soh GH, Rogers KW, Bergmann JK, Bläßle AJ, and Müller P (2017). Dynamics of BMP signaling and distribution during zebrafish dorsal-ventral patterning. eLife 6, e25861. [PubMed: 28857744]

Pyati UJ, Webb AE, and Kimelman D (2005). Transgenic zebrafish reveal stage-specific roles for Bmp signaling in ventral and posterior mesoderm development. Development 132, 2333–2343. [PubMed: 15829520]

Rhinn M, Lun K, Amores A, Yan YL, Postlethwait JH, and Brand M (2003). Cloning, expression and relationship of zebrafish gbx1 and gbx2 genes to Fgf signaling. Mech. Dev 120, 919–936. [PubMed: 12963112]

Rogers KW, and Schier AF (2011). Morphogen gradients: from generation to interpretation. Annu. Rev. Cell Dev. Biol 27, 377–407. [PubMed: 21801015]

Sansom SN, and Livesey FJ (2009). Gradients in the brain: the control of the development of form and function in the cerebral cortex. Cold Spring Harb. Perspect. Biol 1, a002519. [PubMed: 20066088]

Santos D, Luzio A, and Coimbra AM (2017). Zebrafish sex differentiation and gonad development: A review on the impact of environmental factors. Aquat. Toxicol 191, 141–163. [PubMed: 28841494]

Schier AF, and Talbot WS (2005). Molecular genetics of axis formation in zebrafish. Annu. Rev. Genet 39, 561–613. [PubMed: 16285872]

Schmid B, Fürthauer M, Connors SA, Trout J, Thisse B, Thisse C, and Mullins MC (2000). Equivalent genetic roles for bmp7/snailhouse and bmp2b/swirl in dorsoventral pattern formation. Development 127, 957–967. [PubMed: 10662635]

Schmierer B, and Hill CS (2007). TGFbeta-SMAD signal transduction: molecular specificity and functional flexibility. Nat. Rev. Mol. Cell Biol 8, 970–982. [PubMed: 18000526]

Schulte-Merker S, Lee KJ, McMahon AP, and Hammerschmidt M (1997). The zebrafish organizer requires chordino. Nature 387, 862–863. [PubMed: 9202118]

Smith SM, and Maughan PJ (2015). SNP genotyping using KASPar assays. Methods Mol. Biol 1245, 243–256. [PubMed: 25373762]

Smoak EM, Stein P, Schultz RM, Lampson MA, and Black BE (2016). Long-Term Retention of CENP-A Nucleosomes in Mammalian Oocytes Underpins Transgenerational Inheritance of Centromere Identity. Curr. Biol 26, 1110–1116. [PubMed: 27040782]

Suzuki T, Hasso SM, and Fallon JF (2008). Unique SMAD1/5/8 activity at the phalanx-forming region determines digit identity. Proc. Natl. Acad. Sci. USA 105, 4185–4190. [PubMed: 18334652]

Troilo H, Zuk AV, Tunnicliffe RB, Wohl AP, Berry R, Collins RF, Jowitt TA, Sengle G, and Baldock C (2014). Nanoscale structure of the BMP antagonist chordin supports cooperative BMP binding. Proc. Natl. Acad. Sci. USA 111, 13063–13068. [PubMed: 25157165]

Tuazon FB, and Mullins MC (2015). Temporally coordinated signals progressively pattern the anteroposterior and dorsoventral body axes. Semin. Cell Dev. Biol 42, 118–133. [PubMed: 26123688]

Tucker JA, Mintzer KA, and Mullins MC (2008). The BMP signaling gradient patterns dorsoventral tissues in a temporally progressive manner along the anteroposterior axis. Dev. Cell 14, 108–119. [PubMed: 18194657]

Umulis D, O'Connor MB, and Blair SS (2009). The extracellular regulation of bone morphogenetic protein signaling. Development 136, 3715–3728. [PubMed: 19855014]

van Boxtel AL, Chesebro JE, Heliot C, Ramel MC, Stone RK, and Hill CS (2015). A Temporal Window for Signal Activation Dictates the Dimensions of a Nodal Signaling Domain. Dev. Cell 35, 175–185. [PubMed: 26506307]

Wardle FC, Welch JV, and Dale L (1999). Bone morphogenetic protein 1 regulates dorsal-ventral patterning in early Xenopus embryos by degrading chordin, a BMP4 antagonist. Mech. Dev 86, 75–85. [PubMed: 10446267]

Wolpert L (1969). Positional information and the spatial pattern of cellular differentiation. J. Theor. Biol 25, 1–47. [PubMed: 4390734]

Xie J, and Fisher S (2005). Twisted gastrulation enhances BMP signaling through chordin dependent and independent mechanisms. Development 132, 383–391. [PubMed: 15604098]

Yabe T, Shimizu T, Muraoka O, Bae YK, Hirata T, Nojima H, Kawa-kami A, Hirano T, and Hibi M (2003). Ogon/Secreted Frizzled functions as a negative feedback regulator of Bmp signaling. Development 130, 2705–2716. [PubMed: 12736214]

Zagorski M, Tabata Y, Brandenberg N, Lutolf MP, Tkačik G, Bollen-bach T, Briscoe J, and Kicheva A (2017). Decoding of position in the developing neural tube from antiparallel morphogen gradients. Science 356, 1379–1383. [PubMed: 28663499]

Zakin L, and De Robertis EM (2010). Extracellular regulation of BMP signaling. Curr. Biol 20, R89–R92. [PubMed: 20144774]

Zinski J, Bu Y, Wang X, Dou W, Umulis D, and Mullins MC (2017). Systems biology derived source-sink mechanism of BMP gradient formation. eLife 6, e22199. [PubMed: 28826472]

Zinski J, Tajer B, and Mullins MC (2018). TGF-β Family Signaling in Early Vertebrate Development. Cold Spring Harb. Perspect. Biol 10, a033274.

Zinski J, Tuazon F, Huang Y, Mullins M, and Umulis D (2019). Imaging and Quantification of P-Smad1/5 in Zebrafish Blastula and Gastrula Embryos. Methods Mol. Biol 1891, 135–154. [PubMed: 30414130]

Highlights

- Membrane-tethered Chordin can correctly pattern the zebrafish DV axis
- Bmp1a/Tolloid proteases generate a Chordin sink in the dorsal embryo half
- Tolloid is partially redundant to maternal Bmp1a, while Sizzled is dispensable
- Large-scale computational screens reveal principles of BMP gradient formation

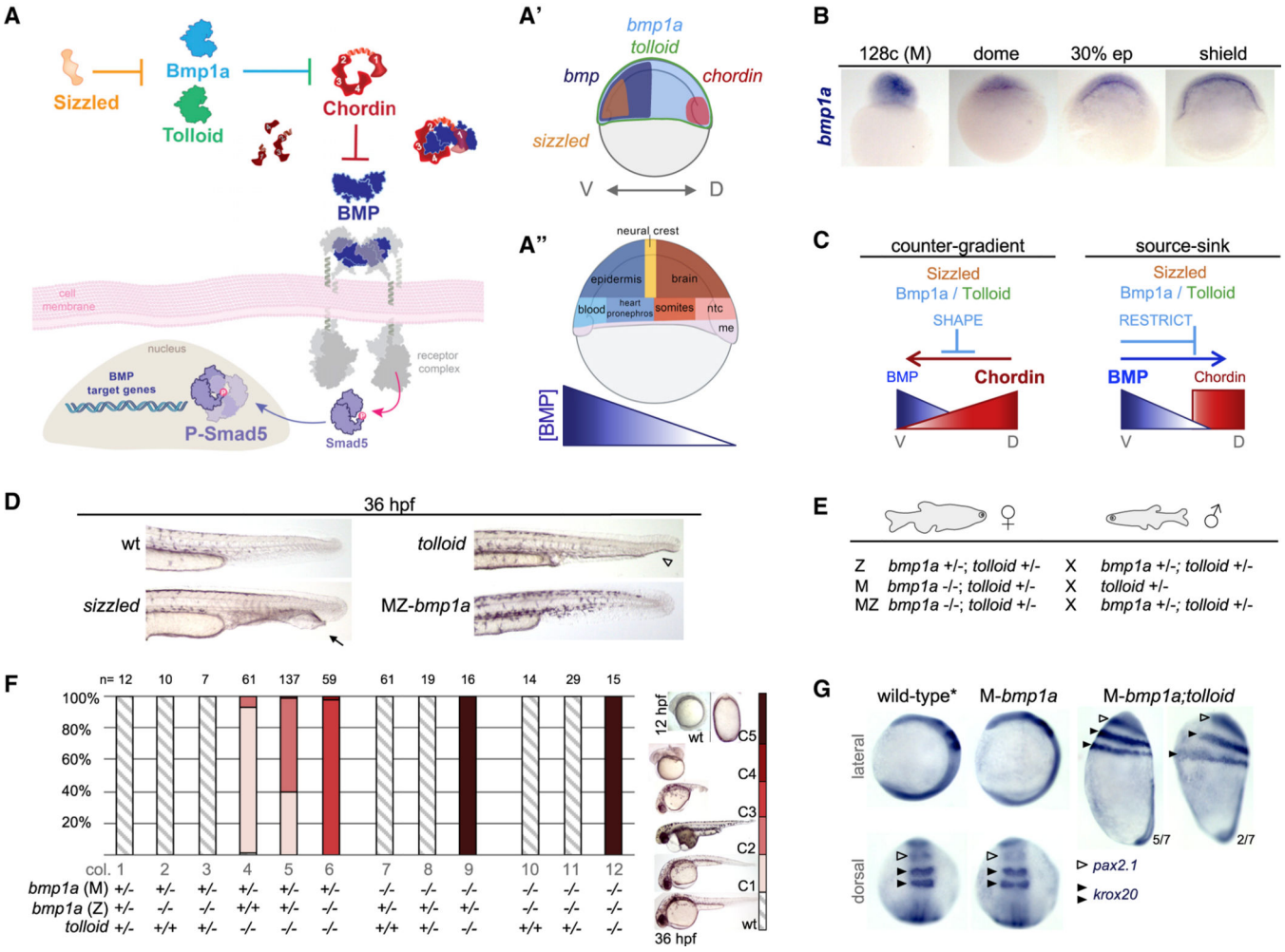

Figure 1. Bmp1a and Tolloid Are Essential for DV Patterning

(A–A″) The extracellular BMP regulators explored in this paper, adapted from Dutko and Mullins (2011), and (A′) their published mRNA expression domains in the zebrafish gastrula (6.3 hpf). (A″) Fatemap of the early zebrafish gastrula (ntc, notochord, me, mesendoderm).

(B) *bmp1a* mRNA expression in wild-type embryos at 128-cell (2.5 hpf), dome (4.3 hpf), 30% epiboly (4.7 hpf), and shield (6.3 hpf) stages. (M, maternal expression).

(C) Distinguishing mechanisms of BMP gradient formation and the roles for metalloprotease regulation therein. In the counter-gradient, long-range Chordin diffusion (red arrow) drives gradient formation, and Bmp1a, Tolloid, and Sizzled shape this Chordin counter-gradient. In the source-sink, BMP diffusion (blue arrow) drives gradient formation, and Bmp1a, Tolloid, and Sizzled instead restrict Chordin dorsally to generate the sink.

(D) Tail phenotypes of wild-type and *tolloid*, *sizzled*, and MZ-*bmp1a* mutants at 36 hpf. Open arrow: loss of ventral tail fin. Solid arrow: duplication of ventral tail fin.

(E) Adult fish crosses used to generate zygotic (Z), maternal (M), and maternal-zygotic (MZ) depletion of *bmp1a* and Z *tolloid*.

(F) Dorsalization of embryos resulting from Z-, M-, and MZ-*bmp1a;tolloid* crosses (columns 1–6, 7–9, and 10–12, respectively). *bmp1a* (M) indicates genotype of the mother, while *bmp1a* (Z) and *tolloid* indicate embryo genotype. n from 2 to 4 replicates.
(G) Lateral view of wholemount *in situ* analysis of neurectoderm markers at 5-somite stage (12 hpf). In wild-type (n = 9) and M-*bmp1a* (n = 4) embryos, *pax2.1* (open arrowhead) is expressed in the forebrain and *krox20* (black arrowheads) in the hindbrain. *Pax2.1* and *krox20* are radially expanded in M-*bmp1a;tolloid* embryos (n = 7). n from 2 replicates, asterisk (*) indicates in-tube controls.
See also Figures S1 and S2.

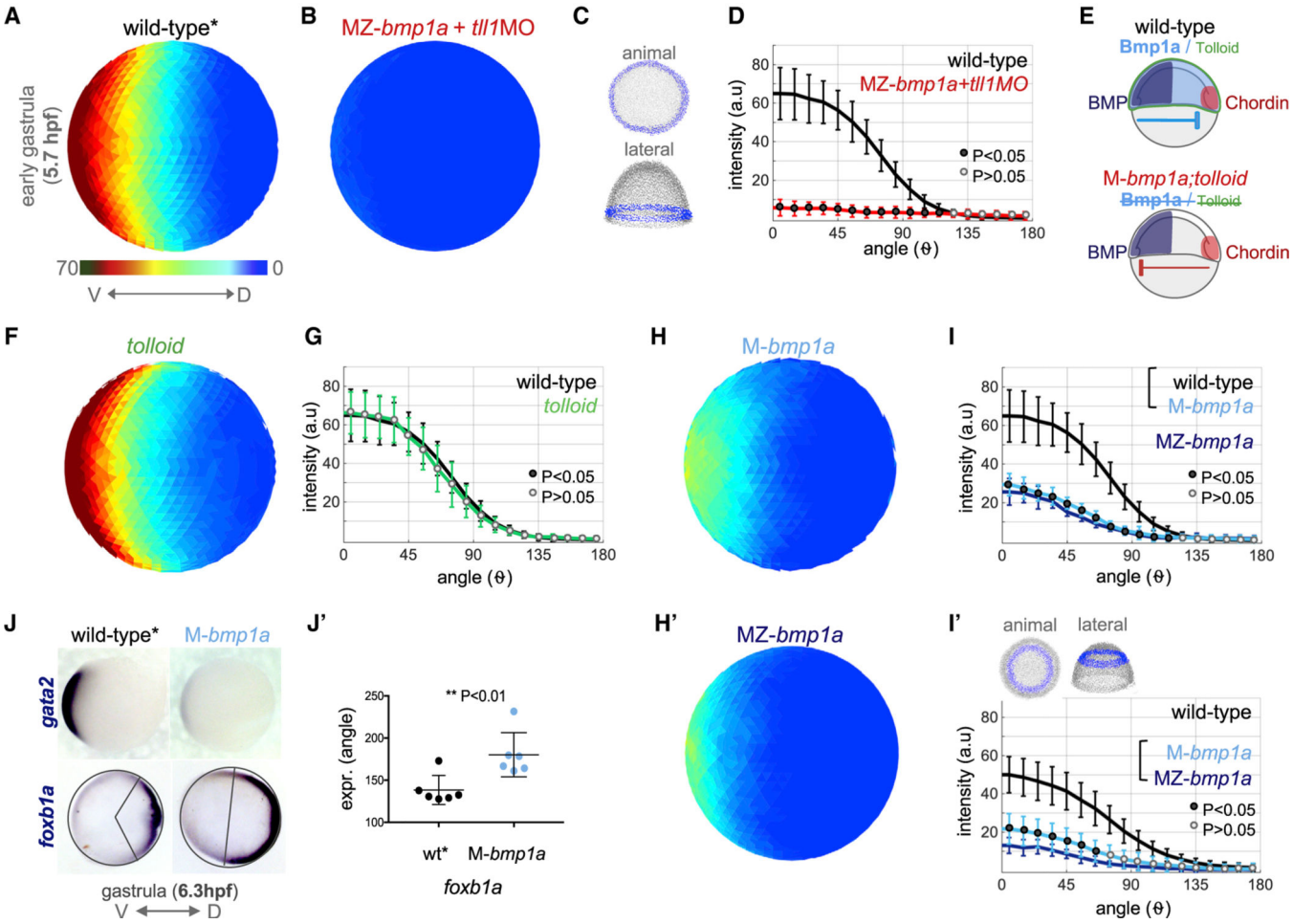

Figure 2. M-Bmp1a Is Required for a Normal P-Smad5 Gradient and Functions Redundantly with Tolloid

Asterisk (*) indicates in-tube controls.

In (A), (B), (F), and (H and H′), animal view of mean P-Smad5 intensities at early gastrula stage (5.7 hpf) is shown.

(A) Wild-type controls (n = 29), pooled from all figure experiments.

(B) MZ-*bmp1a* mutant embryos injected with 2 ng *tll1*MO (n = 9, 2 replicates).

(C) Standard location of 30-μm band of cells used to generate marginal P-Smad5 profiles in (D), (G), and (I).

(D, G, I, and I′) Average P-Smad5 intensities of (A), (B), (F), (H), and (H′). Wild-type controls shown in black. Error bars indicate standard deviation. Filled circles indicate a significant ($p < 0.05$) difference at each position compared to wild type, unless a bracket indicates another comparison. (D, G, and I) Marginal P-Smad5 profiles generated at position in (C); (I′) P-Smad5 profile at indicated animal position.

(E) Our model that Bmp1a/Tolloid normally restrict Chordin dorsally (top) and that in M-*bmp1a;tolloid* mutants (bottom), Chordin is unrestricted and inhibits BMP signaling ventrally.

(F) *tolloid* mutants (n = 10, 3 replicates).

(H and H′) M-*bmp1a* (n = 11, 4 replicates) (H) and MZ-*bmp1a* mutants (n = 8, 2 replicates) (H′).

(J and J′) Animal view of wholemount *in situ* analysis of ventral marker *gata2* (wild type n = 5, M-*bmp1a* n = 10) and dorsal marker *foxb1a* (wild type n = 6, M-*bmp1a* n = 6) at 6.3 hpf (J). Quantification of *foxb1a* angle of expression (J′).

See also Figures S2–S4.

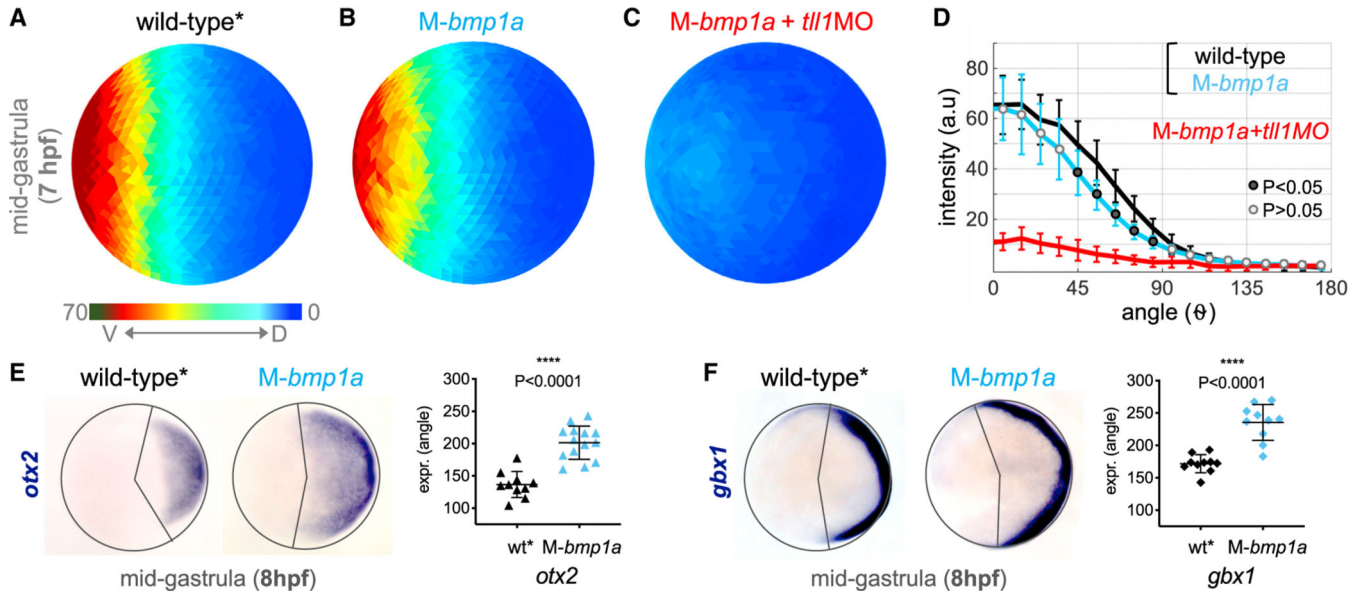

Figure 3. M-*bmp1a* Embryos Rapidly Recover Peak P-Smad5 Levels while Patterning Defects Persist

Asterisk (*) indicates in-tube controls.

(A)–(C) Animal view of mean P-Smad5 intensities at gastrula stage (7 hpf) in the following: (A) wild-type controls (n = 11), pooled from all figure experiments; (B) M-*bmp1a* mutant embryos (n = 6, 2 replicates); and (C) M-*bmp1a* mutant embryos injected with 2 ng *tll1*MO (n = 4).

(D) Average marginal P-Smad5 intensities of (A)–(C). Error bars indicate standard deviation. Filled circles indicate a significant ($p < 0.05$) difference at each position compared to wild type.

(E and F) Animal view and quantification of wholemount *in situ* analysis at 8 hpf of dorsal markers (E) *otx2* (wild type n = 10, M-*bmp1a* n = 14) and (F) *gbx1* (wild type n = 10, M-*bmp1a* n = 10).

See also Figures S4 and S5.

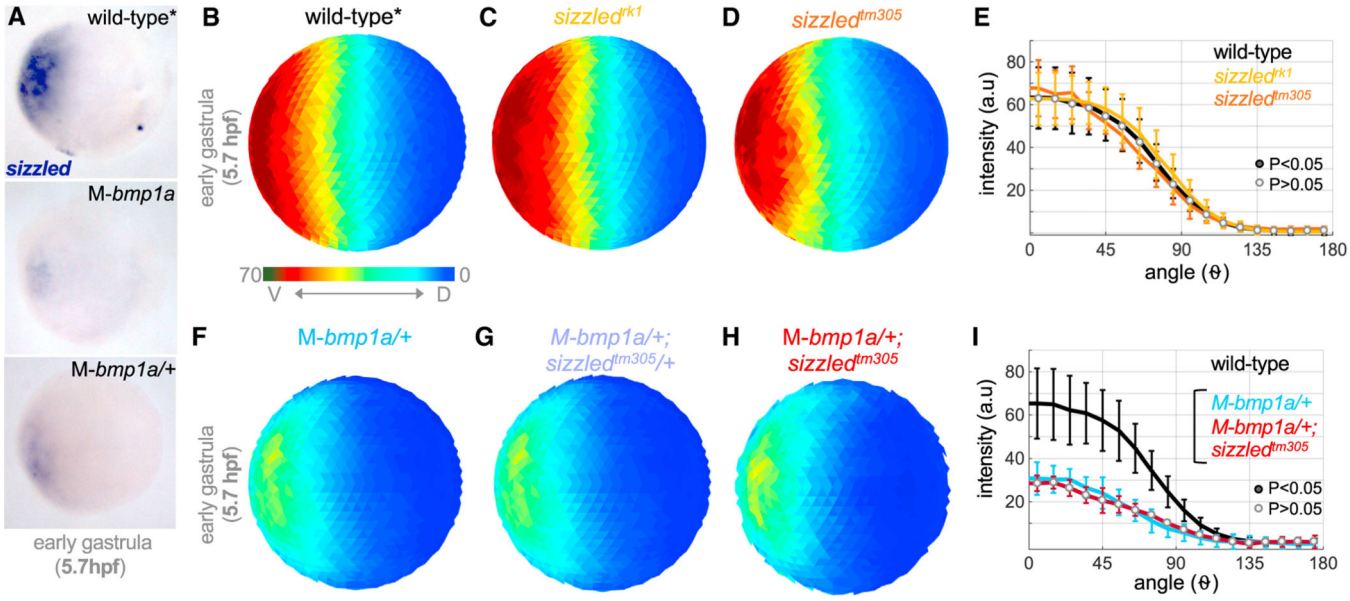

Figure 4. Sizzled Is Dispensable for Early BMP Gradient Formation

Asterisk (*) indicates in-tube controls.

(A) Animal view of wholemount *in situ* analysis of *sizzled* at 5.7 hpf (wild type n = 26, M-*bmp1a* n = 9, M-*bmp1a/+* n = 8).

(B and C) Animal view of mean P-Smad5 intensities at early gastrula stage (5.7 hpf) in (B) wild-type controls (n = 42), pooled from all figure experiments and (C) *sizzled*^{rk1} mutant embryos (n = 34, 3 replicates).

(D) *sizzled*^{tm305} mutant embryos (n = 8, 2 replicates).

(E and I) Average marginal intensities of (B)–(D) or (F)–(H). Wild-type controls shown in black. Error bars indicate standard deviation. Open circles indicate no significant ($p > 0.05$) difference at any position in each mutant compared to wild type or between M-*bmp1a/+* and M-*bmp1a;sizzled* siblings.

(F–H) Animal view of mean P-Smad5 intensities at 5.7 hpf in siblings from a *bmp1a/+;sizzled*^{tm305}/+ female crossed to a *sizzled*^{tm305}/+ male: (F) M-*bmp1a*/+ (n = 4), (G) M-*bmp1a/+;sizzled*/+ (n = 4), and (H) M-bmp1a/+;sizzled (n = 3).

See also Figure S4.

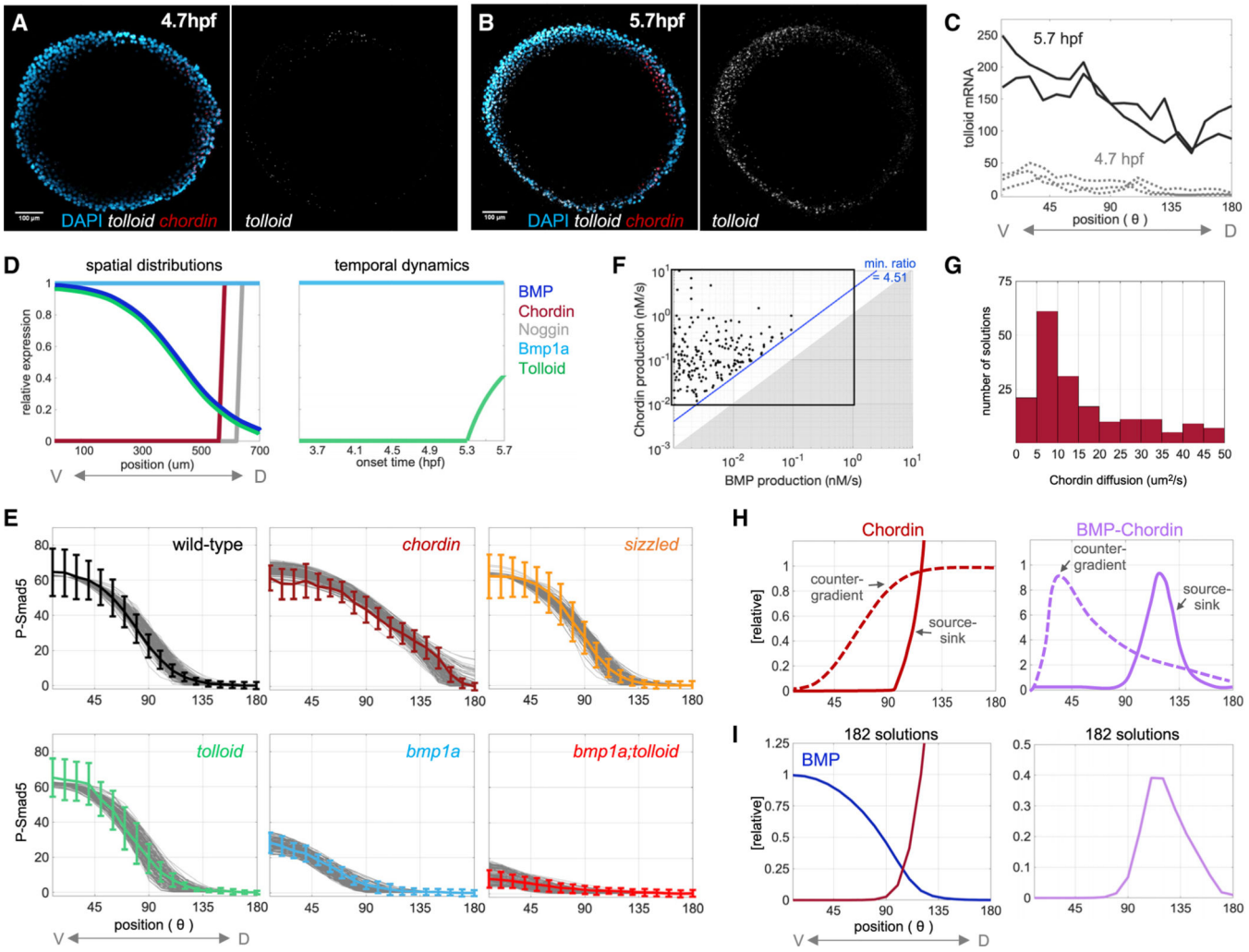

Figure 5. Incorporating Differential *tolloid* and *bmp1a* Expression into a Mathematical Model of BMP Gradient Formation

(A and B) RNAscope analysis of wild-type *tolloid* expression at 4.7 (n = 3) and 5.7 (n = 2) hpf. Scale bars, 100 μm.

(C) Quantification of (A) and (B).

(D) Distinct spatial distribution and temporal dynamics of Bmp1a and Tolloid expression in model input.

(E) BMP distribution (gray lines) in the 182 model solutions under wild-type and the indicated mutant conditions compared to respective measured P-Smad5 profiles. Error bars indicate standard deviation.

(F) Rates of BMP (ϕ_B) and Chordin production (ϕ_C) in the 182 model solutions. Grayed area indicates values excluded by the $\phi_B < \phi_C$ constraint, black box indicates parameter ranges, and blue line indicates the minimum ϕ_C:ϕ_B ratio of 4.51.

(G) Histogram of Chordin diffusion (D_C) rates in the 182 model solutions.

(H) Distributions of free Chordin and BMP bound to Chordin (BMP-Chordin) predicted in the counter-gradient (dashed line) and source-sink (solid line) mechanisms.

(I) Mean Chordin and BMP-Chordin distributions (normalized to maximum BMP concentration) in the 182 model solutions clearly follow source-sink predictions. See also Figure S6 and Tables S1–S5 and S6.

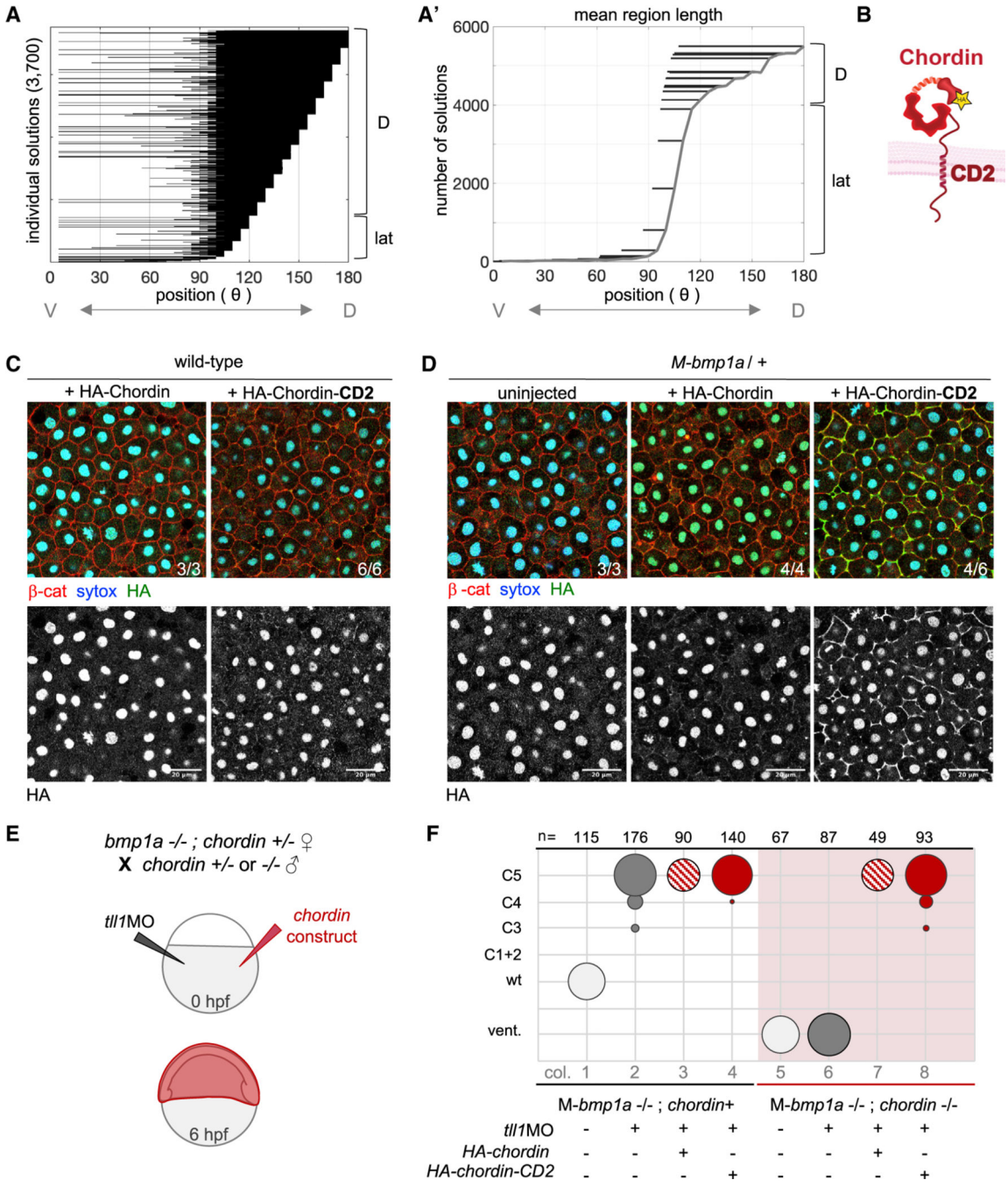

Figure 6. Immobile Chordin Is a Viable Modulator of BMP Signaling

(A and A′) Display of 1/20th of the 73,896 immobile Chordin model screen solutions. Each line represents an individual immobile Chordin domain and was sorted along the *y* axis by its dorsal-most position: 0°–60° was classified as ventral, 61°–120° as lateral (lat), and 121 – 180 as dorsal (D). (A′) Horizontal black lines indicate the mean length of all immobile Chordin regions binned in 5° intervals. The number of solutions within each interval is shown on the *y* axis, and the frequency of solutions is denoted by the solid gray curve. Regions classified as D or lat as in (A).

(B) Schematic of our membrane-tethered Chordin construct with N-terminal HA tag.
(C) Anti-HA immunostaining of wild-type embryos injected at the 1-cell stage with *HA-chordin* or *HA-chordin-CD2* mRNAs (single z-slice, n from 2 replicates, scale bars, 20 μm).
(D) Anti-HA immunostaining of M-*bmp1a*^{sa2416}/+ embryos injected at the 1-cell stage with *HA-chordin* or *HA-chordin-CD2* mRNA (single z-slice, n from 2 replicates, scale bars, 20 μm).
(E) Cross and injection conditions (3 ng *tll1*MO and 250 pg *HA-chordin* or *HA-chordin-CD2*) used to generate (F).
(F) Phenotypes of M-*bmp1a* embryos separated by *chordin* genotype, with M-*bmp1a* and M-*bmp1a*;*chordin*/+ pooled as M-*bmp1a*;*chordin*+. Ubiquitous expression of either HA-Chordin or HA-Chordin-CD2 (columns 7 and 8) resulted in equivalent dorsalization as endogenous Chordin (column 2); n from 3–6 replicates. These injections include the controls performed in parallel to the regional injections in Figures 7D and 7E. Circle size normalized to total number of embryos in each genotype. Circle color represents injection condition: white is un-injected, gray is *tll1*MO only, red stripes are *tll1*MO and *HA-chordin*, solid red is *tll1*MO and *HA-chordin-CD2*.
See also Figure S7 and Table S7.

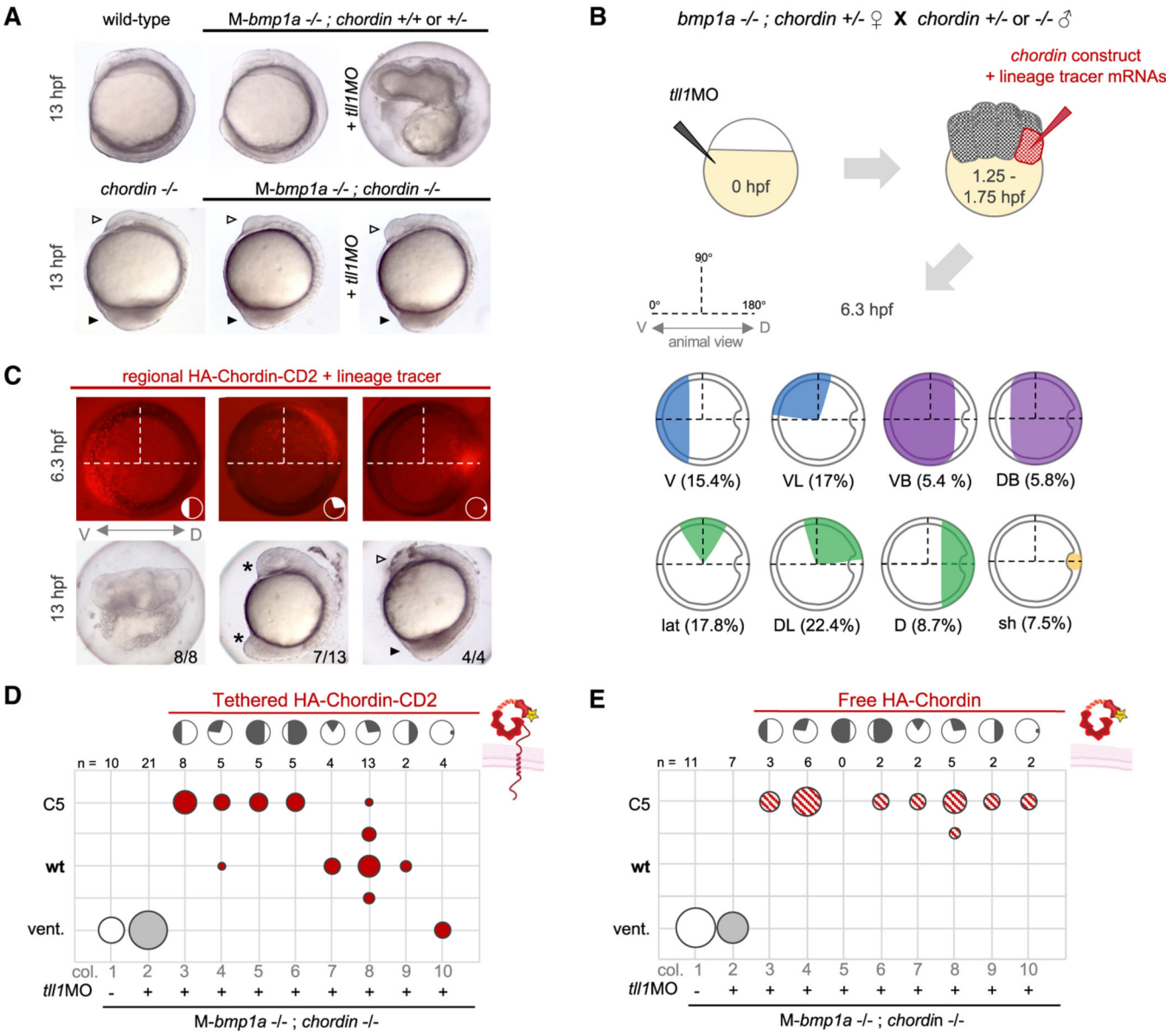

Figure 7. Chordin Mobility Is Dispensable for DV Patterning *In Vivo*

(A) Embryo phenotypes at 13 hpf (8-somite stage). Top: M-*bmp1a* mutants with endogenous *chordin* are wild type. Injection of *tll1*MO causes radial dorsalization, resulting in embryo lysis at this stage. Bottom: the *chordin* mutant ventralized phenotype, characterized by reduced eyes (open arrowhead) and thickening of posterior tissue (black arrowhead), is observed in M-*bmp1a*;*chordin* double-mutant siblings with and without the *tll1*MO (quantified in E, F, and Figure 6F).

(B) Cross and injection conditions (3 ng *tll1*MO and 250 pg *HA-chordin* or *HA-chordin-CD2* mixed with *H3.3-mCherry*) used to generate regional expression, shown in (C) and quantified in (D) and (E). Frequency of each expression region is classified as V (ventral), VL (ventrolateral), VB (ventral broad), DB (dorsal broad), lat, DL (dorsolateral), D, or sh

(shield) at 6.3 hpf (n = 258, 9 replicates, from regional expression embryos in D and E and Figures S7C and S7D).

(C) Representative regional expression at 6.3 hpf and phenotypes at 13 hpf of M-*bmp1a;chordin* double-mutant embryos injected with *tll1*MO and regional *HA-chordin-CD2*. Lineage tracer (H3.3-mCherry) fluorescence marks the HA-Chordin-CD2 expression region. DL expression results in rescue of *chordin* mutant ventralization (middle panel, asterisks).

(D and E) Phenotypes of M-*bmp1a;chordin* double-mutant embryos from regional expression of either *HA-chordin-CD2* (D) or *HA-chordin* (E). DL expression (columns 7–9) of HA-Chordin-CD2 (n from 6 replicates), but not HA-Chordin (n from 3 replicates), rescued the ventralized *chordin* mutant phenotype. Circle size normalized to total number of embryos in each panel. Circle color represents injection condition: white is un-injected, gray is *tll1*MO only, red stripes are *tll1*MO and *HA-chordin*, and solid red is *tll1*MO and *HA-chordin-CD2*, with the expression regions schematized above the graph.

See also Figure S7.

KEY RESOURCES TABLE

REAGENT or RESOURCE	SOURCE	IDENTIFIER
Antibodies		
Rabbit monoclonal anti-Phospho-Smad1/5/8	Cell Signaling Technology	Cat# 13820; RRID: AB_2493181
Goat anti-rabbit Alexa Fluor 647	ThermoFisher	Cat# A-21244; RRID: AB_141663
Sytox Green	ThermoFisher	Cat# S7020
Rabbit polyclonal HA tag antibody	ThermoFisher	Cat# 71-5500; RRID: AB_2533988
Mouse IgG1 monoclonal anti-β-catenin	BD Biosciences	Cat# 610153; RRID: AB_397554
Goat anti-rabbit Alexa Fluor 594	ThermoFisher	Cat# A-11037; RRID: AB_2534095
Goat anti-mouse Alexa Fluor 633	ThermoFisher	Cat# A-21126; RRID: AB_2535768
Critical Commercial Assays		
DIG RNA Labeling Kit	Roche	11277073910
SP6 mMESSAGE mMACHINE Transcription Kit	ThermoFisher	Cat# AM1340
KASP Master Mix	LGC Biosearch Technologies	Cat# 1016
RNAscope Pretreat 3	Advanced Cell Diagnostics	Cat# 320045
RNAscope Fluorescent multiplex detection reagents	Advanced Cell Diagnostics	Cat# 320851
Deposited Data		
Segmented individual and mean P-Smad5 embryo data	This paper	Mendeley Data: https://doi.org/10.17632/xtk7yyxt5f.
Parameter values for 182 solutions to final model screen (10 million simulations)	This paper	Table S6
Experimental Models: Organisms/Strains		
Zebrafish: wild-type (TU)	Mary Mullins Lab	ZIRC_ZL57
Zebrafish: *chordin*^{tt250}	Mary Mullins Lab	ZDB-ALT-980413-523, ZIRC_ZL61
Zebrafish: *tolloid*^{tm124a}	Mary Mullins Lab	ZDB-ALT-001220-2, ZIRC_ZL464
Zebrafish: *bmp1a*^{t31169} (TU)	Matthew Harris Lab; Bowen et al., 2012	ZDB-ALT-061101-360, EZRC_9002
Zebrafish: *bmp1a*^{t31169} (TU+AB)	This paper	N/A
Zebrafish: *bmp1a*^{sa2416}	Zebrafish Mutation Project, Sanger Institute	ZDB-ALT-120411-333
Zebrafish: *sizzled*^{tk1}	National BioResource Project Zebrafish, RIKEN	ZDB-ALT-030530-2
Zebrafish: *sizzled*^{tm305}	Mary Mullins Lab	ZDB-ALT-980203-1563, ZIRC_ZL830, EZRC_750

REAGENT or RESOURCE	SOURCE	IDENTIFIER
Zebrafish: *bmp1a*^{t31169};*tolloid*^{tm124a}	This paper	N/A
Zebrafish: *bmp1a*^{sa2416};*tolloid*^{tm124a}	This paper	N/A
Zebrafish: *bmp1a*^{t31169};*sizzled*^{tm305}	This paper	N/A
Zebrafish: *bmp1a*^{t31169};*chordin*^{tt250}	This paper	N/A
Oligonucleotides		
Morpholino: MO1-*tolloid* GCAGAGTAAAGGTAGTCCATCTGAG	Gene Tools	ZDB-MRPHLNO-041217-9
KASP primer assay: *chordin*^{tt250} GTTTGGTGTGATGCACTGCGTTATGTGTCATTGTGAGCCG[G/A]TGAGTTGTGCACAGTTCAGTTTGAAATCCATATTGAATCT	LGC Biosearch Technologies	N/A
KASP primer assay: *tolloid*^{tm124a} TGGAGGAGTCATCCCTTACGTCATAGGAGGCAACTTCACC[G/T]GTAAGAGGACTAAGTGTTTGCCTTTTCAGCATCAATGTGT	LGC Biosearch Technologies	N/A
KASP primer assay: *bmp1a*^{t31169} GCACACGCGACCCGACAGAGACGAACACGTCAGTATCATA[C/T]GAGACAACATTCAGCCAGGTAGGAGAAAAAAACTGTAGGG	LGC Biosearch Technologies	N/A
KASP primer assay: *bmp1a*^{sa2416} CGAGAGGCATGATAACTGTGCGTACGACTACCTGGAGGTT[C/T]GAGACGGGAACTCRGAAAGCAGCCCGCTTTTGGGCAGGTT	LGC Biosearch Technologies	N/A
KASP primer assay: *sizzled*^{tk1} CCTTCGTCTGCTCGCTCATCGCCCCTGTATGCCTCGACAG[G/A]TACGTGTTGAGACACCTAAAATATTATGAGAAATACACAT	LGC Biosearch Technologies	N/A
Sizzled^{tm305} genotyping forward primer: 5'-CCTCGATCTGACGACTTGAGGA-3'	IDT	Yabe et al., 2003
Sizzled^{tm305} genotyping reverse primer: 5'-GCCAGTTCTAAATCATGAGCTACAC-3'	IDT	Yabe et al., 2003
Recombinant DNA		
pCS2+ HA-Chordin	This paper	N/A
pCS2+ HA-Chordin-CD2	This paper	N/A
pCS2+ H3.3-mCherry	Mary Mullins Lab	Smoak et al., 2016
Software and Algorithms		
ImageJ	https://imagej.nih.gov/ij/	N/A
MATLAB	Mathworks	N/A
Algorithms for P-Smad5 gradient analysis	Zinski et al., 2017, 2019	N/A
Computational model of BMP gradient formation	This paper	https://github.com/xiaoweiwei20/FiniDiffModel-of-BMP-signaling-in-zebrafish
LALIGN	Chojnacki et al., 2017	https://www.ebi.ac.uk/Tools/psa/lalign/
Excel	Microsoft	N/A
Prism8	GraphPad	N/A
Other		
RNAscope probe – *chordin*	Advanced Cell Diagnostics	Cat# 440081

REAGENT or RESOURCE	SOURCE	IDENTIFIER
RNAscope probe – *tolloid*	Advanced Cell Diagnostics	Cat# 475501-C2
Anti-sense RNA probe – *bmp1a*	Masahiko Hibi Lab	Muraoka et al., 2006
Anti-sense RNA probe – *sizzled*	Masahiko Hibi Lab	Yabe et al., 2003
Anti-sense RNA probe – *chordin*	Mary Mullins Lab	Miller-Bertoglio et al., 1997
Anti-sense RNA probe – *pax2.1 (pax2a)*	Mary Mullins Lab	Krauss et al., 1992
Anti-sense RNA probe – *krox20*	Mary Mullins Lab	Oxtoby and Jowett, 1993
Anti-sense RNA probe – *foxb1a (fkd3, foxb1.2)*	Mary Mullins Lab	Odenthal and Nüsslein-Volhard, 1998
Anti-sense RNA probe – *gata2*	Mary Mullins Lab	Detrich et al., 1995
Anti-sense RNA probe – *otx2*	Mary Mullins Lab	Li et al., 1994
Anti-sense RNA probe – *gbx1*	Mary Mullins Lab	Rhinn et al., 2003